8-30-2011

Fracture toughness of ultra high performance concrete

Ebadollah Honarvar Gheitanbaf

Ebadollah Honarvar Gheitanbaf
_____
Candidate

Civil Engineering
_____
Department

This thesis is approved, and it is acceptable in quality
and form for publication:

Approved by the Thesis Committee:

_____ ,Chairperson

_____

_____

_____

_____

_____

_____

_____

_____

_____

FRACTURE TOUGHNESS OF ULTRA HIGH PERFORMANCE CONCRETE

BY

EBADOLLAH HONARVAR GHEITANBAF

B.SC. IN CIVIL ENGINEERING
UNIVERSITY OF TEHRAN, TEHRAN, IRAN

THESIS

Submitted in Partial Fulfillment of the
Requirements for the Degree of

**MASTER OF SCIENCE
Civil Engineering**

The University of New Mexico
Albuquerque, New Mexico

July, 2011

DEDICATION

To My Parents

ACKNOWLEDGMENTS

I would like to express my sincerest gratitude to Dr. Arup Maji, my advisor, and the chair of my thesis committee for endowing me this unique opportunity to accomplish my research and obtain the MS degree under his supervision.

I would like to thank my thesis Committee members: Dr. Walter Gerstle, who was always there to help me with his priceless recommendations, taught me to ponder critically about the problems in the tests, and Dr. Mahmoud Reda Taha with whom I took the Fracture Mechanics course. His vast knowledge of fracture mechanics built my theoretical foundation of this subject.

This research would have not been possible without the help of Kenny Martinez, the structural laboratory supervisor. He was always more than willing to provide all the necessary materials for my tests.

I would like to thank Scott Chapman, a graduate student, for helping me conduct the fracture tests, and Andrew Garner, a graduate student, for his cooperation in casting Ultra-High Performance Concrete (UHPC).

FRACTURE TOUGHNESS OF ULTRA HIGH PERFORMANCE CONCRETE

BY

EBADOLLAH HONARVAR GHEITANBAF

ABSTRACT OF THESIS

Submitted in Partial Fulfillment of the
Requirements for the Degree of

MASTER OF SCIENCE
Civil Engineering

The University of New Mexico
Albuquerque, New Mexico

July, 2011

Fracture Toughness of Ultra-High Performance Concrete

By

Ebadollah Honarvar Gheitanbaf

M. S. in Civil Engineering, University of New Mexico

Albuquerque, NM, USA 2011

B. Sc. in Civil Engineering, University of Tehran

Tehran, Iran 2009

ABSTRACT

In this study, fracture properties of Ultra-High Performance Concrete (UHPC), and High Performance Concrete (HPC) are presented. The average compressive strengths of UHPC and HPC used in the tests were 141 MPa, and 55 MPa respectively. Formulation and processing of the mixes and test specimens are also presented. Size effect and the influence of compressive strength of concrete on fracture parameters were investigated using test methods recommended by ACI Committee 446.

The Fracture properties investigated included crack opening displacement (COD), fracture energy G_F, fracture toughness K_{IC}, and bilinear approximation of the softening curve, for two different sizes of UHPC and HPC.

TABLE OF CONTENTS

LIST OF TABLES

LIST OF FIGURES

CHAPTER 1

INTRODUCTION

1.1   Introduction

The subject of Fracture mechanics encompasses crack initiation and propagation. Many structures fail due to cracks, and it is essential to realize the significance of the fracture in the real life to avoid catastrophic failures. It has been observed that neither linear elastic fracture mechanics (LEFM) nor elastic plastic fracture mechanics (EPFM) can be applied to concrete. The complexity arises from the fact that, different toughening mechanisms exist in the fracture process zone (FPZ) of concrete to consume energy. This led to use of quasi-brittle fracture mechanic (QBFM) to characterize the fracture parameters of concrete. The cohesive pressure which tends to close the crack is assumed to model the toughening mechanisms in the FPZ by QBFM. As a result, the factitious crack approach was proposed by Hillerborg et al. for fracture of concrete [1], which was the basis for test methods proposed by RILEM. Later investigation revealed that the fracture parameters obtained were size dependent. In order solve this size dependency of fracture properties; ACI Committee 446 proposed new test methods which does not have any size effect.

The ultra-high performance concrete is known for high compressive strength which results in poor fracture toughness. The brittle fracture of UHPC makes the

use of ultra-high performance fiber reinforced concrete (UHPFRC) very popular. Poor fracture properties of UHPC has inspired research to characterize its fracture parameters, including the wedge splitting test [**2**].

The lack of research on fracture mechanics of UHPC based on the new ACI test method led to this study where the fracture parameters of UHPC for two sizes were determined. Also, the influence of compressive strength on the fracture properties and size-effect of concrete were investigated using High Performance Concrete (HPC).

1.2   Objectives

The primary objectives in this study were:

- To determine the fracture properties of ultra-high performance concrete with no fibers using the new test method proposed by ACI Committee 446.

- To investigate the size effect of the proposed test method on the fracture properties of both UHPC and HPC for two different sizes.

- To investigate the influence of compressive strength of concrete on the fracture properties of concrete for two different sizes.

1.3   Outline of Thesis

Chapter 2 provides a literature review of UHPC, HPC, fracture mechanics of concrete, and the conventional test methods as well as the new test method proposed by ACI Committee 446. Chapter 3 describes how UHPC and HPC were cast as well as the composition of the mix design. It also represents the provisions determined by ACI Committee 446 on how to conduct the Notched Beam Level 2 test. The results and the discussions are mentioned in chapter 4. Eventually, chapter 5 shows the conclusions for this study.

CHAPTER 2

2   LITERATURE REVIEW

2.1   Ultra High Performance Concrete (UHPC)

Concrete can be classified based on its compressive strength as below [3]:

- Conventional concrete up to C53/65.

- High Performance Concrete C53/65 to C90/105.

- Ultra High Performance Concrete C90/105 to C200/230.

One of the major breakthroughs in concrete technology in the last two decades is the development of ultra-high-performance concrete with high compressive strength, also known as Reactive Powder Concrete, which also enhanced the durability in comparison with HPC.

Sustainable lightweight concrete constructions are now made possible by using sufficient amount of steel fibers in UHPC.

2.1.1   UHPC Advantages and Disadvantages

Advantages

- The very dense material structure results in high durability and smaller concrete cover.

- The stress loss in pre-stressing steel is less due to less shrinkage.

- More slender structures are possible which reduces the weight.

- Higher pre-stressing is possible.

- It is possible to construct without steel reinforcement.

Disadvantages

- UHPC is more expensive than conventional concrete.

- UHPC with steel fibers cannot be recycled as the steel fibers can hardly be taken out.

- The hydration process within UHPC is fast which results in a large heat production. This results in a fast hardening shrinkage during the first days. Variable temperatures during hardening within the concrete result in internal stresses causing cracks, particularly important for thick construction elements.

- The production capacity of a concrete mixing plant decreases for the production of UHPC as The mixing takes longer and is more complicated.

- There is a lack of sufficient knowledge about fatigue of the material.

2.1.2 History of Development and Applications of Ultra High Performance Concrete

In the 1960s, under specific laboratory conditions, concretes with compressive strength of up to 800 N/mm^2 were produced. They were cured thermally and compacted under high pressure. Later, in the early 1980s the idea of using concrete with fine aggregate, and dense, and homogenous cements matrix to avoid micro cracks in structures, was developed. Ultra High Performance Concrete is also known as Reactive Powder Concrete (PRC). This is because of the restriction in grain size which limits the size to be less than 1 mm, and also, due to high packing density caused by the addition of various reactive or inert minerals [4].

It was only after 1980, that UHPC was used commercially for the first time for the development of so called D.S.P. mortars in Denmark [5], which was primarily used for special applications in the security industry – like vaults, strong rooms and protective defense constructions.

Greater application of UHPC began around 1985, including heavily reinforced UHPC precast elements for the rehabilitation of deteriorated concrete bridges and industrial floors [5], ductile fiber reinforced fine grained "Reactive Powder Concrete" (RPC), such as "Ductal" produced by Lafarge in France or Densit produced in Denmark [6]. Besides, coarse grained UHPC with natural or artificial high strength aggregates were developed, which might be used for highly loaded columns such as in extremely high-rise buildings [7] . Nowadays a large range of

formulations exist which should be adjusted to meet the specific requirements of an individual design, architectural or construction approach.

Other applications include the very first pre-stressed hybrid pedestrian bridge at Sherbrooke, Canada in 1997, two 20.50 and 22.50 m long road bridges at Bourg-lès-Valence, France, built in 2001 [**8**] and the toll-gate of the Millau Viaduct in France (Figure 2.1) [**9**].

Figure 2.1: Roof of the Millau toll-gate [9]

2.1.3 UHPC Mix Design

The mix design of UHPC is complex; with a low water-cement ratio and many additives. The mix is relative dry, which makes it hard to mix all the materials together. By adding super plasticizers the workability of the mix can be ensured. It is important to divide the additives and fillers into doses to the mix and at the

right time. This however results in a longer mixing time. The UHPC composition is very sensitive to little variations in the amount of materials and is also influenced by the weather conditions. Considering all this it is assumed best to utilize precast UHPC elements instead of in-situ UHPC as this ensures a better quality. However, the utilization of in-situ UHPC is not impossible. Special attention should be paid to the curing of the UHPC because of its very low or even total absence of bleeding. The outer skin and construction joints should be checked and cured to prevent drying out of the concrete causing micro cracks.

However, in order to get a proper mix design for UHPC, it's essential to make the following changes to normal concrete mix design:

- Increasing the package density, by filling the voids with fine particles which can contribute to the strength as well as brittleness.
- Adding steel fibers; this leads to small crack distances and gives the material large ductility. Reducing the water-cement ratio which increases the material strength.
- Improving the homogeneity, by using small sized particles to decrease the stress variation. This also reduces the transverse tensile stresses. A more homogeneous material results in a more homogeneous stress distribution and thus in a generally stronger material.
- Improving the microstructure by hardening the concrete at higher temperatures and/or by hardening at higher pressures.

2.2   High Performance Concrete (HPC)

Although the main focus of this paper is to determine the fracture parameters for UHPC, High Performance Concrete (HPC) was cast in two different sizes as well to study the size effect, and fracture parameters for two different concrete with different compressive strengths.

2.2.1   Background

ACI defined High-Performance Concrete (HPC) as a concrete meeting special combinations of performance and uniformity requirements that cannot always be achieved routinely using conventional constituents and normal mixing, placing, and curing practice. [**10**] The primary applications of High-performance concrete have been in tunnels, bridges, and tall buildings for its strength, durability, and high modulus of elasticity. Moreover, HPC has been used in shotcrete repair, poles, parking garages, and agricultural applications.

2.3   Fracture Mechanics

There are basically two reasons which generally cause failure in structures:

1- "Negligence during design, construction, or operation of structure."

2- "Application of a new design or material, which produces an unexpected results" [**11**].

2.3.1 Historical Perspective

In 1892, early elasticity analysis by Love showed the necessity of understanding crack propagation. Later, in 1920, Griffith made a connection between fracture stress and flaw size [**12**]. Work done by Irwin and Orowan revealed the limitation of Griffith approach for metals, which led them to suggest the energy release rate as fracture criteria [**13**], [**14**].

In 1960, the fundamentals of linear elastic fracture mechanics (LEFM) were fairly well established. Later, Wells suggested the displacement of crack faces as an alternative criterion when significant plasticity precedes failure [**15**]. In 1968, Rice proposed the J-integral as another fracture criterion to better characterize nonlinear behavior of material ahead of the crack by assuming plastic deformation to be nonlinear elastic [**16**].

2.3.2 Fracture Mechanics of Concrete

The stress-strain curve is always linearly elastic up to the maximum stress for an ideally brittle material. For a quasi-brittle material like concrete there is significant non-linearity before the maximum stress. Strain softening can be observed under

stable propagation of the crack. If a closed loop displacement controlled test machine is used, both opening of the crack and unloading of the specimen can be observed for post peak part of the stress-strain curve [17].

Fracture mechanics assumes that an initial crack starts propagating at the proportional limit f_y, and keeps propagating in a stable manner until the peak stress, so new crack surfaces are formed by extension of cracks. It is well established that two fracture criteria govern cracking of concrete [18], [19]:

- Energy criteria: Crack extension requires energy release.
- Stress criteria: crack extension needs stress to overcome the cohesive strength of material.

Although these two criteria can explain the fracture behavior of concrete, the complexity is how to determine what is exactly consuming the energy.

The difference between brittle and ductile material in fracture behavior originates from shape and dimension of the fracture process zone (FPZ), which is a volume of material that is engaged in the formation of new surfaces.

The difficulties in applying fracture mechanics to a quasi-brittle materials like concrete arise from the various toughening mechanism in the FPZ of these materials such as crack bridging, crack branching, crack deflection, crack face friction, crack tip blunting, and micro cracking [17], [20], [21].

Although Glucklich et al. tried to use liner elastic fracture mechanics (LEFM) for concrete [22], the large FPZ limits the application of LEFM. This was shown by

Moavenzadeh and Kuguel in 1969, who observed large differences between theoretical and experimental results [23].

Due to limitation of LEFM, researchers investigated the applicability of elastic-plastic fracture mechanics (EPFM) to concrete. However, most of research was aimed at fiber reinforced concrete (FRC) which has significant non-linearity [24].

Two main parameters of fracture for EPFM are the crack tip opening displacement (CTOD) and the J-integral. Kumar proposed that CTOD is a suitable fracture parameter to characterize the non-linear behavior within the FPZ of concrete, which can be evaluated by measuring the crack mouth opening displacement, assuming a linear crack profile [25].

The J-integral for a non-linear elastic material is defined as the energy available for crack extension; the line integral is used to calculate the J-integral [16].

In 1973, Rice et al. suggested a method to determine J_{IC} for metals using two notched un-notched specimens under pure bending [26].

Later Mindess et al. applied this method in evaluating J_{IC} of fiber reinforced composites using a four point bending test setup [27].

The cohesive pressure is assumed by quasi-brittle fracture mechanics (QBFM) to be acting on the crack surfaces to model different toughening mechanisms in the FPZ, as a modified version of the plastic zone model based on the Dugdale and Barenblatt assumptions [28], [29].

The cohesive pressure σ(w) which tends to close the crack decreases as the crack opening displacement (COD) increases. Based on the cohesive crack model, the energy release rate can be divided into two parts: the energy consumed in separating two surfaces G_{IC} , and the energy consumed to overcome the cohesive pressure σ(w).

$$G = G_{IC} + \int_0^{CTOD} \sigma(w)dw \qquad\qquad\qquad 2.1$$

The first term in the above equation is basically the Griffith LEFM energy balance, while the second term shows the Dugdale-barenblatt correction for plastic materials. Also the shape of the cohesive pressure is a distinction between a quasi-material and plastic material. This model leads to two different approaches in modeling the fracture mechanics of concrete:

2.3.3 The Fictitious Crack Approach

Hillerborg et al. suggested a fictitious crack model for fracture of concrete [1].

If the pre peak tensile response of concrete is ignored, one can consider only the post-peak fracture behavior or softening as below:

13
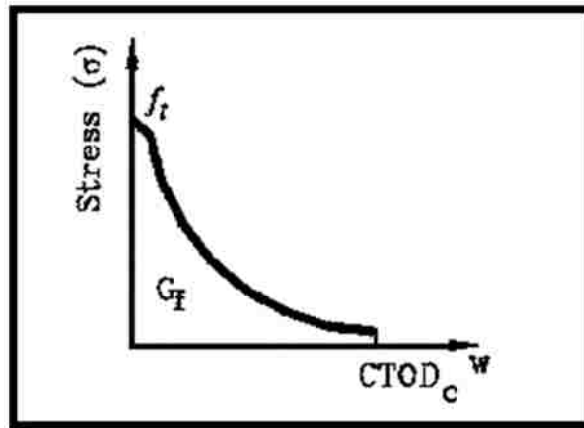
Figure 2.2: Stress-crack opening displacement curve [17]

The area under the entire softening stress-crack displacement curve is G_F, the fracture energy of concrete. This method assumes that the energy consumed in creating new surfaces is negligible compared to the energy consumed in separating surfaces, in other words G_{IC} is zero, while all the energy is consumed in the FPZ, thus:

$$G_F = \int_0^{CTOD_c} \sigma(w)dw \qquad\qquad 2.2$$

It was proposed that the stress-crack displacement curve is a material property that is independent of geometry and size of structures. There exist different models to quantify the amount of energy dissipated in the FPZ such as linear, bilinear, tri-linear, and exponential functions. For instance, CEB-FIP proposed a bilinear curve for σ(w) as below [**30**]:
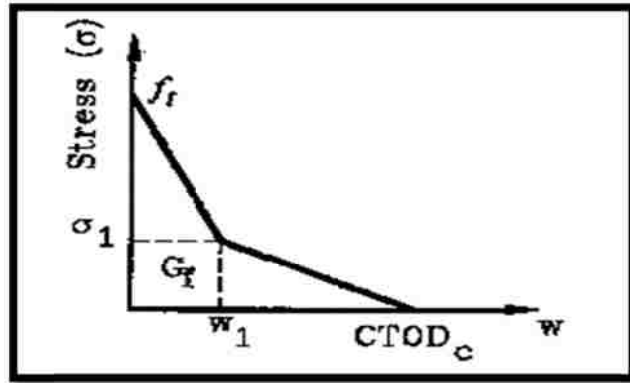
Figure 2.3: Stress-crack displacement curve [30**]**

$$\sigma(w) = \begin{cases} f_t - (f_t - \sigma_1)\left(\dfrac{w}{w_1}\right) & w \leq w_1 \\ \sigma_1 - \sigma_1\left(\dfrac{w-w_1}{w_c-w_1}\right) & w \geq w_1 \end{cases}$$ **2.3**

Where w_1 is an intermediate crack opening displacement, w_c is equal to $CTOD_c$, σ_1 is an intermediate stress corresponding to w_1, and f_t is the tensile strength of material.

2.3.4 The Effective Elastic Crack Approach

This model applies Griffith-Irwin energy dissipation methods to model the fracture process zone in concrete, by assuming that σ(w) is zero [**12**], [**14**]. In fact, the effective elastic crack approach models the FPZ by using an equivalent traction-free elastic crack, which is governed by LEFM criteria.

$$G_F = G_{IC}$$ **2.4**

15

One of the most famous model based on the above discussed principles is two parameter fracture model by Jenq and Shah [**31**] , which includes the critical crack tip opening displacement ($CTOD_c$) , and the stress intensity factor K_{IC} as the two fracture criteria.

2.3.5 Fracture Mechanics of Ultra High Performance Concrete

Concrete becomes more brittle as its compressive strength increases. Thus, UHPC is a brittle material due to high compressive strength, which leads to low fracture energy. That is why usually fibers are used in UHPC to enhance its fracture behavior [**32**].

It was observed that flexural tensile strength increases linearly with increase of fiber volume. Also, the inverse analysis method for determination of a tensile fracture model of UHPFRC was applied and a tri-linear softening curve is suggested based on the primitive curve.

In another paper, the authors investigated the replacement of micro steel fibers steel fibers, and the consequent effects on the fracture behavior of UHPFRC. The two parameter fracture mechanics was used to determine the fracture behavior. The results revealed that only by using undulated or end-hooked steel fibers of 30 or 40 mm in length, the fracture toughness will be similar to that of micro steel fibers [**33**].

In 2003, a study was executed on fracture toughness of ultra-high strength concrete with axial compressive strength of more than 140 MPa. The mix used was similar to the UHPC mix design in this paper, and the mechanical properties mentioned was very close to UHPC. The common fracture parameters such as fracture energy, fracture toughness, characteristic length, and crack opening displacement (COD) were evaluated using the wedge split testing, for two different sizes of aggregates. The authors concluded that, the coarser aggregate enhanced the fracture behavior of UHPC, since UHPC without coarse aggregate, while exhibiting high compressive strength is very brittle [2].

2.4   Experimental Procedures to Calculate Fracture Properties of Concrete

2.4.1 Background

Due to the presence of a large fracture process zone in concrete, conventional methods based on LEFM cannot be applied directly to measure fracture parameters. RILEM committee has recommended three drafts to compute fracture parameters of concrete [34], which are very briefly discussed here; they are based on the fictitious crack model by Hillerborg et al. [1], the two parameter fracture model by Jenq, and Shah [31], and the size effect model by Bazant et al. [35].

2.4.2 Method of Hillerborg, G_F

This method evaluates G_F using the three-point bend beam, based on the fictitious crack model by Hillerborg et al. **[1]**. The Fictitious crack model includes three fracture parameters: fracture energy G_F, critical crack separation displacement w_c, and material tensile strength, f_t. This method can only determine fracture energy G_F.

Size of the beam depends on the maximum size of aggregate, d_a. The notch depth is equal to half beam depth, and notch width at the tip should be less than 10mm.
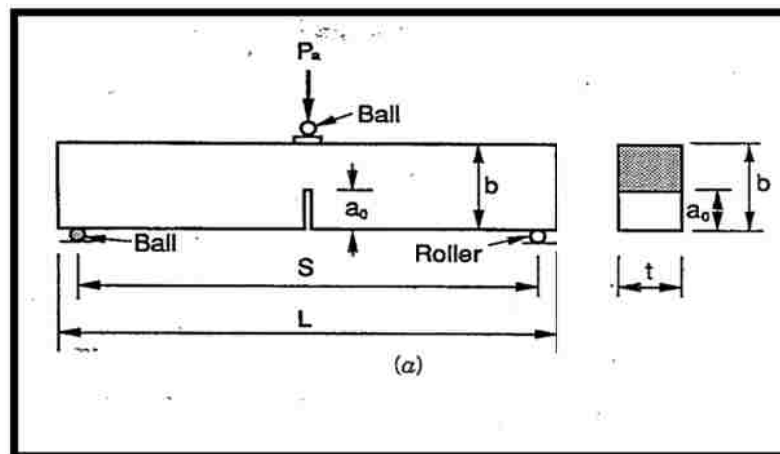
Figure 2.4: The three-point bend beam [17]

The specimens should be loaded under a constant rate of deformation, such that the maximum load is achieved in 30-60 seconds. The relation between load and load point displacement, (LPD) should be recorded and non-elastic deformation

at supports and loading points should be eliminated. A closed loop servo control testing machine is required. The main assumption in this method is that, energy absorption takes place only in the FPZ, i.e., deformation outside this zone is purely plastic.

Test results and calculation

The calculation is based on the recorded load-LPD curve from the test.
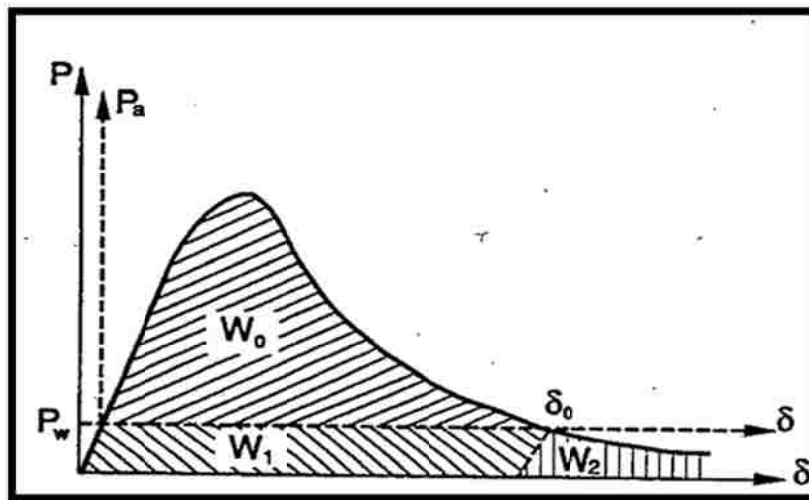
Figure 2.5: Load- displacement curve (Downward load and displacement)
[17]

Then total work of fracture can be calculated as below:

$W_t = W_o + 2P_w\delta_o$

Where,

P_a: Load applied by the machine

P_w: Self weight

W_o: Area below the measured P_a-δ curve

$W_1 = P_w * δ_o = W_2$

Thus, the fracture energy will be:

$$G_F = \frac{W_t}{(b-a_0)t} = \frac{W_0 + 2P_w δ_0}{(b-a_0)t}$$

2.5

Discussion and Conclusion

This method is size independent, and no counterweights are used in the test setup which affects the stability of test. Moreover, the fictitious crack model is based on three fracture parameters, so if only a single parameter is obtained, erroneous conclusion can be made. This is illustrated in the figure below, where the value of G_F is plotted as a function of compressive strength. It indicated that the fracture toughness increases as the material compressive strength increases, which can be shown to be wrong based on the brittleness index which combines the three fracture parameters [**17**].
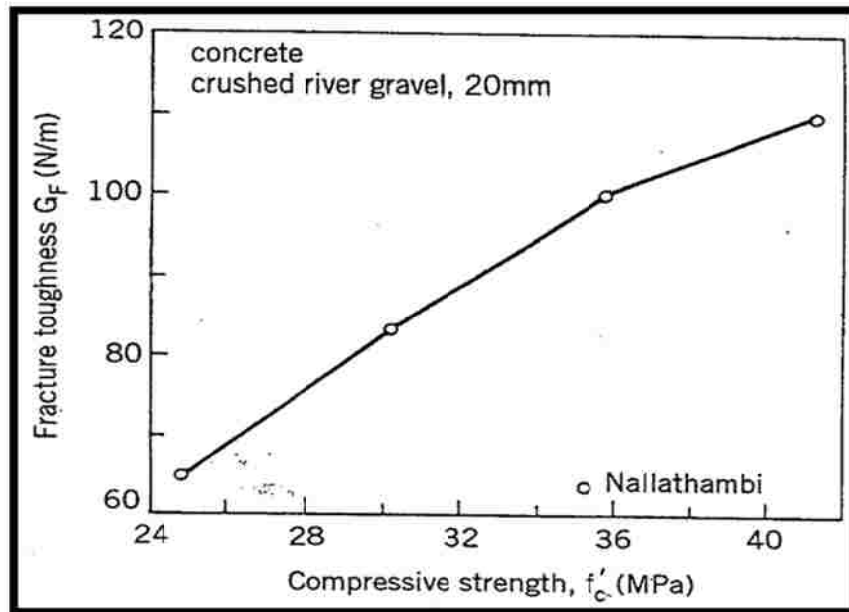
Figure 2.6: Effect of compressive strength of concrete on fracture toughness G$_F$ [36]

2.4.3 Method of Jenq and Shah, K$_{IC}$ and CTOD$_c$

The RILEM Technical Committee 89-FMT on fracture mechanics of concrete-Test Methods recommended three-point bend beam to evaluate, K$_{IC}$, CTOD$_c$, based on the two parameter fracture model by Jenq and Shah [**31**].

Size of the beam depends on the maximum size of aggregate, d$_a$. The notch to depth ratio is 1/3, and notch width at the tip should be less than 5 mm.
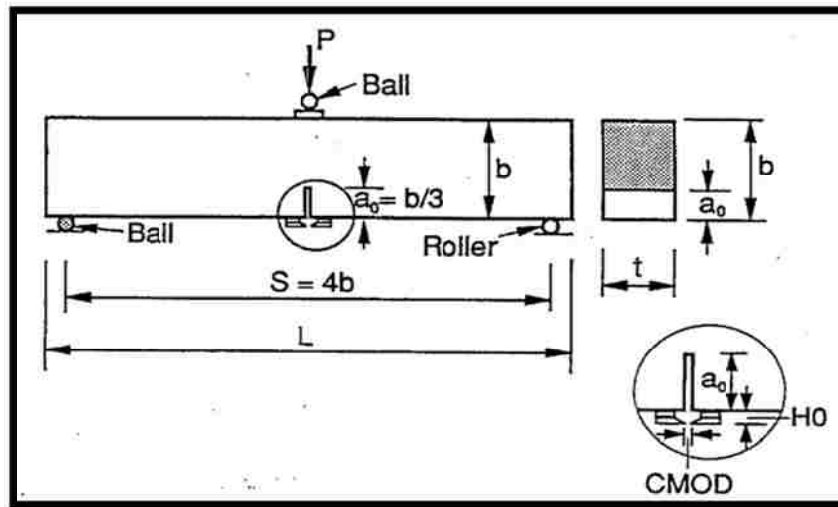
Figure 2.7: The three-point bend beam [17]

A closed loop servo control testing machine is required with crack mouth opening displacement (CMOD) feedback. The specimens are loaded axially, and the peak load should be reached in about 5 minutes. Meanwhile the relationship between load and CMOD should be recorded, and the applied load is manually reduced after it passes the peak load.
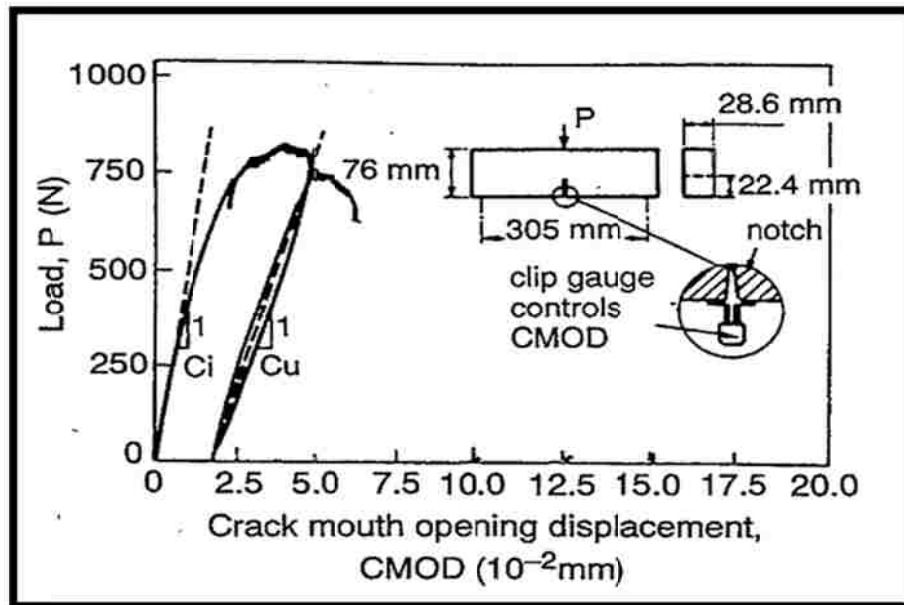
Figure 2.8: Typical load-CMOD curve [17]

Discussion and Conclusion

The values of the critical stress intensity factor, K_{IC}^s changes with variation of beam depth, while it's generally agreed that K_{IC}^s is essentially specimen size independent.

The values of $CTOD_c$ have much greater scatter than values of K_{IC}^s. This could be attributed to:

1. Machine Stability: determination of $CTOD_c$ is very sensitive to precision of the measurement; for large-size specimen the testing machine may not be stiff enough to attain a stable failure. Unloading at peak load will result in extra post-peak crack extension.

23

2. Self-weight: Compensation for self-weight during specimen handling for large-size specimen. The self-weight of the beam may already preload and damage the beam before loading.

In the aforementioned method, the effects of self-weight and machine stability were not addressed, since the specimens are relatively small.

3. $CTOD_c$ Calculations:

In this model $CTOD_c$ is based on the elastic compliance at the peak load, While:

$$CTOD_c = CTOD_c^e + CTOD_c^p$$

Where, $CTOD_c^e$ is the elastic component of CTOD$_c$, and $CTOD_c^p$ is the plastic component of CTOD$_c$.

The unloading procedure is used, so that $CTOD_c^p$ can be subtracted from $CTOD_t$. $CTOD_c^p$ has a greater portion in $CTOD_t$ for small-size specimen because the fracture process zone is larger compared to specimen size.

2.4.4 RILEM Method of Bazant G_F and c_f

The RILEM Technical Committee 89-FMT on fracture mechanics of concrete-Test Methods recommended the three-point bend beam to evaluate G_F, based on the size effect model by Bazant et al. [35].

Specimens of at least three different sizes are needed, and the specimens should be loaded at a constant displacement rate, so the maximum load is reached in 5 minutes. Other details are illustrated in the figure below:
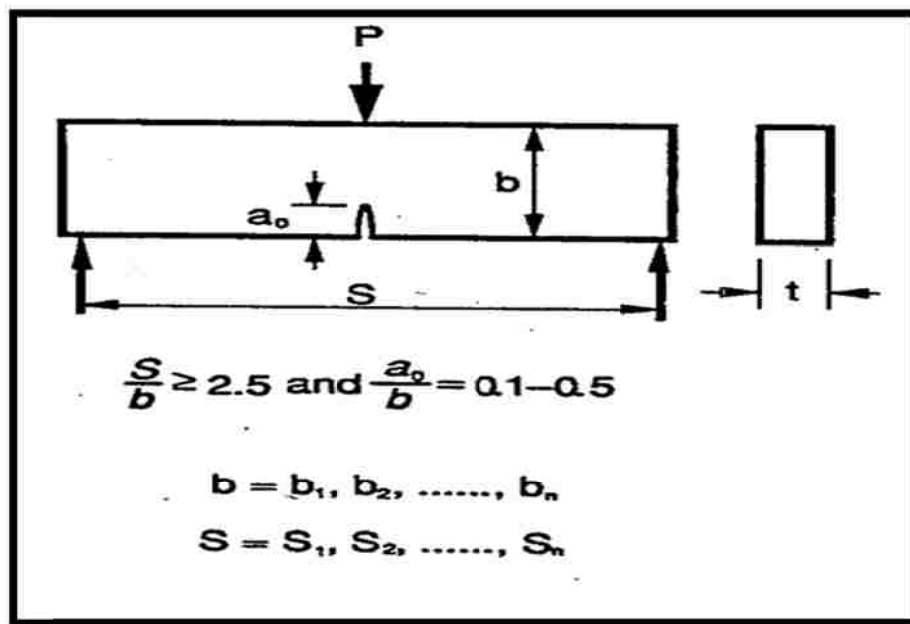
Figure 2.9: The three-point bend beam [17]

This method provides the values for fracture energy, G_f, and the length of the fracture process zone, c_f.

Discussion and Conclusion

- G_f obtained corresponds to fracture energy dissipated in an infinitely large specimen, thus it is independent of specimen size.

- G_f is obtained from an extrapolation of the peak loads of finite-size specimen by statistical regression.

2.4.5 Summary and Comparison of the Three Methods

The differences and similarities between three different test methods can be summarized into:

- G_f is based on the size effect model.

- G_{Ic}^s is obtained indirectly from K_{Ic}^s and E as $G_{Ic}^s = (K_{Ic}^s)2/E$.

- G_{Ic}^s, and G_f are both based on effective-elastic crack approach.

- G_F is based on the fictitious crack model, and its roughly twice as great as G_{Ic}^s, and G_f, Because G_F is based on global load and the LPD curve.

- In calculating G_F, true surface separation energy is considered as well as spurious energy and energy dissipated outside of the fracture process zone. In addition, the energy required to form the fracture process zone is also included.

- G_F is averaged by the whole ligament area at the crack front which includes both areas inside and outside of the fracture process zone. But the other two methods represent the energy dissipated on a unit crack area in the fracture process zone.

2.5   ACI Committee 446: Fracture Toughness Testing of Concrete

2.5.1 Introduction

After consideration of the many proposed test methods, ACI Committee 446, "Fracture Mechanics" suggested two laboratory tests for characterizing the fracture behavior of concrete. Both of the proposed fracture tests use identical geometry and loading: a notched beam loaded in three-point bending. These two proposed tests are the most suitable candidates as possible ASTM standard tests [37].

The first test, is a Level I test (requiring only measurement of peak loads), whereas the second, is a Level II test, requiring a closed-loop testing machine. The Level I test may be used, for example, to determine the initial portion of a stress-crack opening displacement curve. It can also be used to determine the parameters of different size effect models. The second test is a Level II test, capable of determining an estimation of the entire stress-crack opening versus displacement curve. It can also be used to determine the parameters of the two-parameter fracture model.

The laboratory tests described here purposefully contain no theoretical interpretation. The parameters of several different fracture models can be evaluated from the results of the two tests. The precision and bias of these fracture toughness tests are not still determined.

Test method used in this paper to determine fracture mechanics behavior is the Level II (Closed Loop) Notched Beam Test. This method follows the original work by Guinea [**38**].

Later, various equations will be used to determine the fracture parameters. Therefore it is essential to understand how and on what basis these equations are derived. To obtain a brief insight to the theory behind the equations, the forgoing discussion is provided which basically revolves around the principals of cohesive crack model.

2.5.2 Background

The complete softening curve is essential to characterize the cohesive crack model. It is observed that, while the direct tension test is the best way to get this softening curve, but the difficulties in performing the test limited the further use of this method. Therefore, different methods were proposed to replace the direct tension test, the very first method was proposed by RILEM based on cohesive crack model, which used the work of fracture to calculate fracture parameters [**34**]. The results from the tests revealed the size dependency of fracture parameters, which could be due to either flaw in experimental method or limitation of model or both.

Planas and his coworkers investigated the test procedure and analysis, and came into conclusion that enhancement of experimental method can decrease

the size effect on G_F. They also believed that, the remaining size effect is due to rough formulation of the cohesive crack model. Hence, the suggested method is actually an approximate method to calculate the fracture energy based on approximate model. This is analogous to determination of Young's modulus of concrete. Concrete is not a linear elastic material.

The value of G_F provides a good evaluation of concrete toughness, but this value alone does not provide enough information for analyzing structures. G_F can be more helpful if it is combined with other information about the softening curve such as the tensile strength f_t. However, this is still not sufficient to obtain good prediction about structure unless the shape of the softening curve is also determined which again emphasizes the significance of cohesive crack model by Hillerborg.

2.5.3 Determination of the Initial Part of the Softening Curve

The initial portion of the softening curve which, for concrete, can usually be estimated by a straight line totally controls the peak load of not too large specimens. Guinea, Planas and Elices used that [38] for determining the initial slope of the softening curve from the determination of the peak load, as follows [39]:

The following geometry was considered: a three-point bend beam with a span-to-depth ratio of 4, and an initial notch-to-depth ratio, α_0 equal to 0.5. Furthermore, it

is assumed that a bending test is used and only the peak load P_U is measured (The necessary correction was accounted for compensation of specimen self-weight), After some mathematical manipulation (For more details see [**39**]). l_1, and w_1 are determined as below:

$$l_1 = \frac{D}{X}(0.15755 - 0.25677\Delta\alpha - 0.22136\Delta\alpha^2) \qquad \textbf{2.6}$$

$$w_1 = \frac{2f'_t l_1}{E} \qquad \textbf{2.7}$$

It should be noted that, the above equation for l_1 holds if the beam span to depth ratio is four, while the test setup for ACI Committee 446 is based on the beam span to depth ratio of 3.

2.5.4 Determination of Fracture Energy, G_F

Hillerborg and the RILEM Committee 50 recommended the simplest methods of determining the fracture energy for concrete [**1**], [**34**], by work-of-fracture. See Section 2.4.2.

The fracture energy based on the cohesive crack model recommendation is defined as the energy required for producing a unit area of crack (fully broken).Thus, if the specimen is broken statically, and the related work of fracture W_F is measured, then the approximate fracture energy can be formulated as below:

$$G_F = \frac{W_F}{b(D-a_0)}$$
2.8

Although at the first glance, the above equation may seem overly simplistic, in fact, the application of concept makes it really complicated. For instance, a stable machine is needed to measure the static work of fracture, and also ensuring that the energy in consumed in the fracture process zone rather than elsewhere (For more specific details see 3.3).

One of the main issues in determining the work of fracture is the self-weight compensation. If the test setup is uncompensated, the work of fracture (W_0) can be calculated as the shaded area in Figure 2.10 which is basically what is recorded during the test. This calculated area is in fact significantly smaller than the total work of fracture which is the area A'AMBTB'A"A'. Hence area A'ABTB'A"A' must be added to W_0. Area A'AMBTB'A"A' can be subdivided into two smaller areas: the area A'ABB'A"A' which is equal to P_0u_0, where u_0 is the recorded load-point, and minus small triangle A'AA", and the area B'BTB', which was proven by Petersson to be equal to P_0u_0 as well [40].
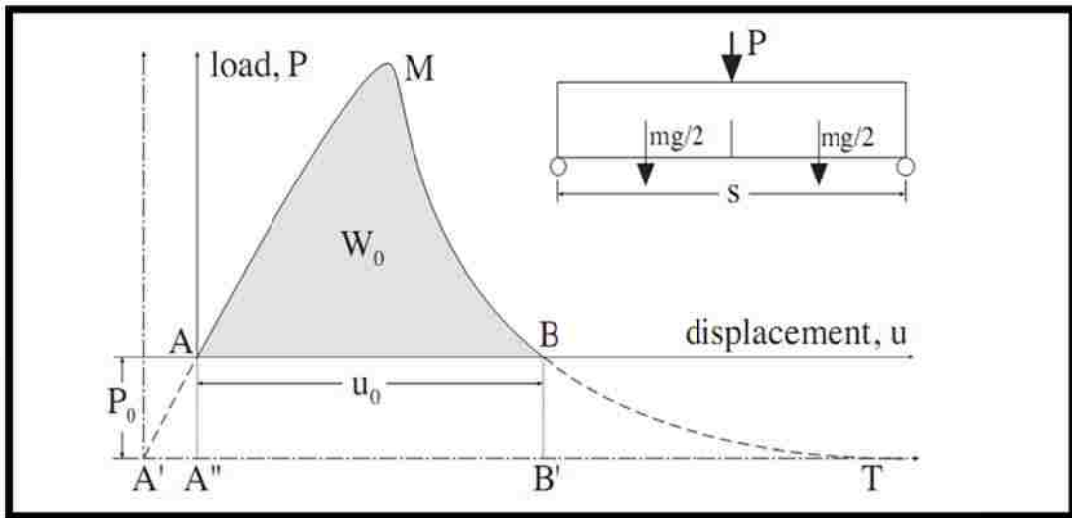
Figure 2.10: Load-displacement curves for uncompensated three-point bending test [39]

$$W_F = W_0 + 2 P_0 u_0 \qquad\qquad\qquad\qquad \textbf{2.9}$$

For a simple case, P_0 can be assumed to be equal to mg/2, while in more general case P_0 is calculated as the central load that produces the same central bending moment as the system of dead loads:

$$P_0 = \frac{4M_0}{S} \qquad\qquad\qquad\qquad \textbf{2.10}$$

Where M_0 is the central bending moment produced by the dead-loads (including the self-weight of the specimen and fixtures resting on the specimen) and S is the loading span.

Petersson assumed that at point B the specimen is very close to complete failure [**40**]. But, for large specimens, P_0 can be a significant fraction of the peak load

32

which contradicts the assumption of point B being close to complete failure. Thus, the full softening curve should be obtained instead of just calculating the last portion done by Petersson. Different methods are suggested to add weight compensation to test setups which are sketched in Figure 2.11:

- Using specimens twice as long as the loading span (Figure 2.11).

- Attaching dead-weights (Figure 2.11).

- Using springs to attach the central part of the specimen to the loading head (Figure 2.11). It should be noted that when these springs are used, the tension force in the springs is larger than P_0 as determined before, and the length of the springs will not change with deformation of the specimen.
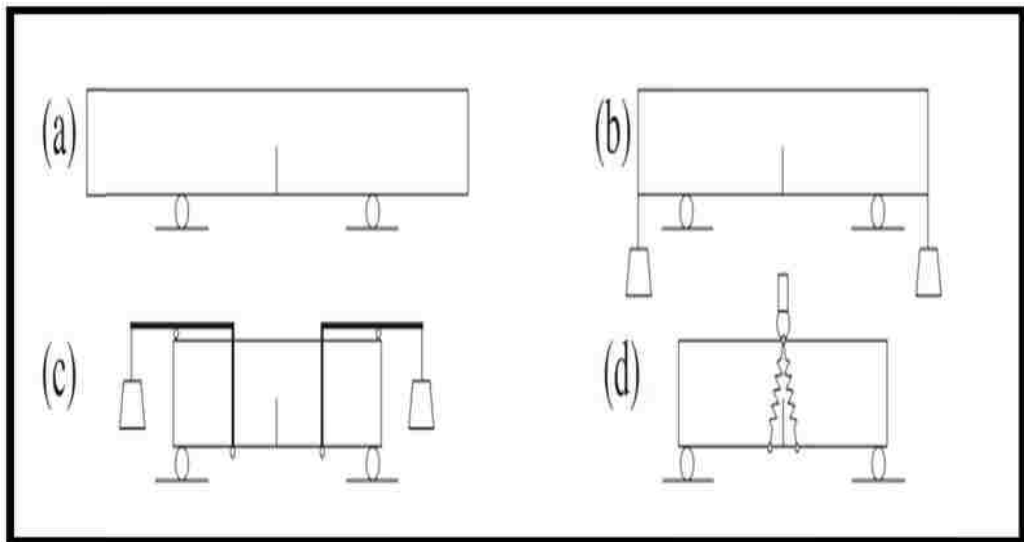
Figure 2.11: Weight compensation devices: (a) longer specimens, (b) dead weights, (c) lever with dead weights, (d) spring attachment [39]

It is recommended to have a slight overcompensation in practice which produces a negative bending moment. So at the end of test dead force P corresponds to a certain positive constant load P'_0. The load displacement curve is shown in Figure 2.12, with exaggeration in value of P'_0.

P'_0 is an unknown parameter in advance before performing the test, but it can be measured after the test on the load displacement record itself as shown in Figure 2.12. The shaded area in Figure 2.12 represents the work of fracture which is enclosed between the curve, and the line A'T drawn parallel to the displacement axis through the last point of the record T (The point at which the specimen fails and is fully broken).
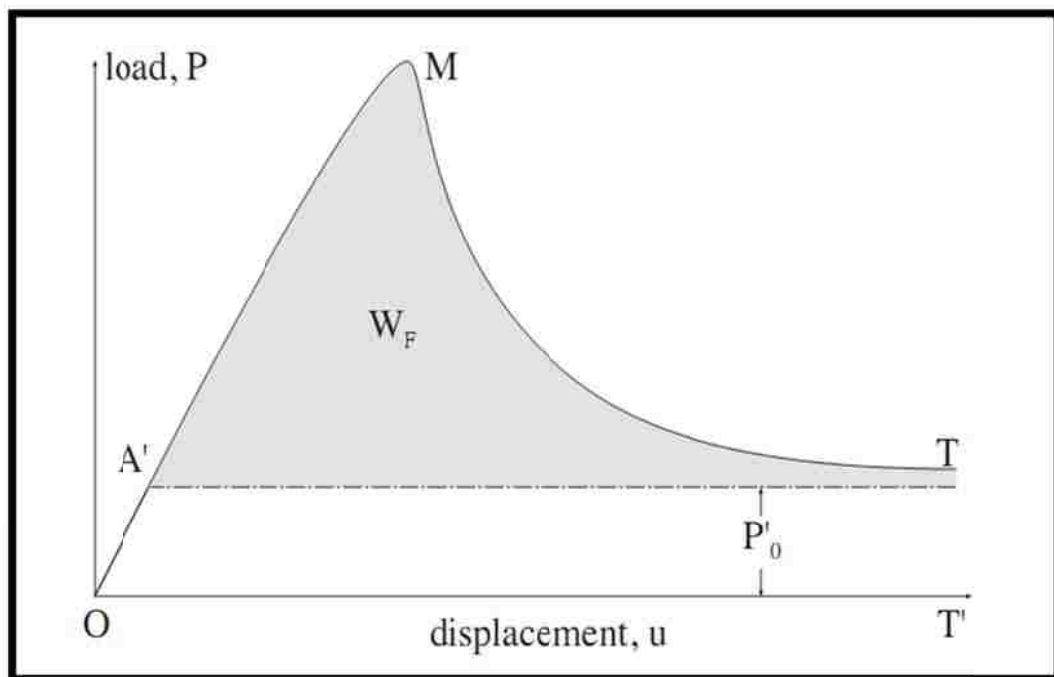
Figure 2.12: Load-displacement curves for overcompensated three-point bending test in an ideal situation (at T, the specimen is fully broken) [39]

At the first glance, the above discussion may seem adequate for the bending test failure, whereas in fact a complete failure in the bending test occurs asymptotically. This implies that point T is infinitely far, and the test should be terminated before most energy is dissipated. Hence, the actual picture is shown in Figure 2.13, where you can see the area which indicates that the work of fracture is shifted up compared to the original curve and now the last recorded test data point is B, which lies a small distance P'$_B$ above the true complete failure asymptote. Also, the area A'ABTB'A can be calculated based on the method of Hillerborg and Petersson to find P'$_B$ which is indeed small. Finally, the total work of fracture can be calculated as below:

$$W_F = W_m + 2P'_B u'_B \qquad P'_B = P_B - P'_0 \qquad \qquad \textbf{2.11}$$
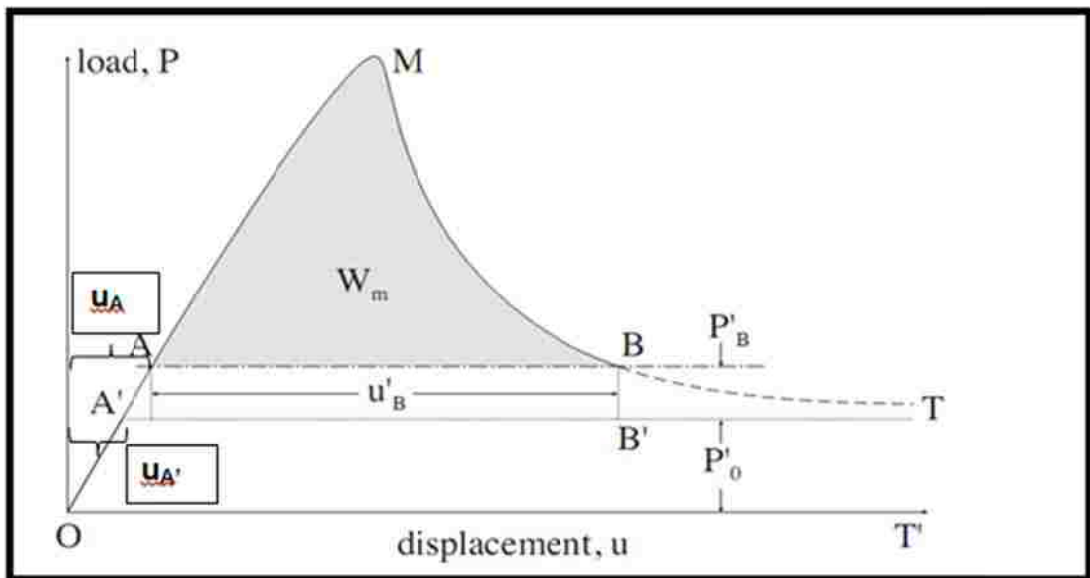
Figure 2.13: Load-displacement curves for overcompensated three-point bending test in a real situation. (The test is stopped at B, before the specimen is fully broken [39])

35

Where $u'_B = u_B - u_{A'} = u_B - u_A$ (note that the points A and A' lie on the elastic line, and so $u_A - u_{A'} << u_B$) It is essential to realize that, P'_B, is not known well, and should be estimated.

Petersson proposed that the load-displacement curve, behaves asymptotically with u^{-2}:

$$P - P'_0 = \frac{A}{(u-u_A)^2}$$ **2.12**

Where A is a constant ($N\text{-}mm^2$), P and u are the recorded data from test, and u_A can be determined by interpolation. Then, if the duration of test was long enough, this equation can be applied to the last part of the curve, to calculate P'_0 and A using a least-square fit to the data [**39**].

The curve can be modified to be precisely satisfied by the last point B, since in fact, P'_0 is not an essential parameter. So it can be rewritten as

$P_B - P'_0 = P'_B = A / (u_B - u_A)^2$, which leads to

$$P - P_B = A\left(\frac{1}{(u-u_A)^2} - \frac{1}{(u_B-u_A)^2}\right)$$ **2.13**

Therefore, if $P - P_B$ versus $(u-u_A)^{-2} - (u_B-u_A)^{-2}$ is plotted, the value for A can be evaluated by fitting a quadratic equation or line.

Once A has been determined, the total work of fracture can be calculated as below:

$$W_F = W_m + 2\frac{A}{u_B - u_A}$$ **2.14**

2.5.5 Determination of a Bilinear Softening Curve

The bilinear curve which describes the softening behavior of concrete can be approximated by using data from the cylinder splitting test, and stable fracture test [**38**]. Brazilian test can provide good approximation of f'_t, and the values for w_1 and G_F can be determined from the peak load of the stable facture test and the area under the softening curve respectively. Also, a relationship between constant A and the abscissa of the center of gravity, w_G can be established. As a result of determining all the four aforementioned parameters, the complete bilinear softening curve can be plotted.

The purpose of the following equations is to find a relationship between the tail constant A and the center of gravity of the softening curve. Petersson's rigid-body estimation of the kinematics of the beam at the stages close to the failure is sketched in Figure 2.14. The two halves of the beam are assumed to be rigid and connected together by a cohesive zone, so that the crack opening is calculated by:

$\omega = 2\theta x$ **2.15**

Where x is the displacement measured from top of the beam as shown in Figure 2.14, and θ is the rotation of each half of the specimen (Assuming small value of θ).
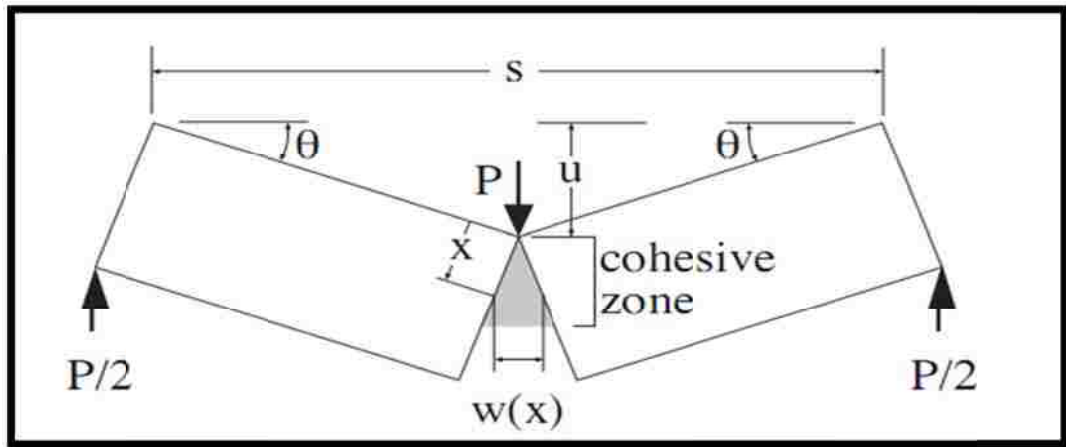
Figure 2.14: Rigid body kinematics towards the end of the test (adapted from Elices, Guinea and Planas 1992). [39]

Now the moment equilibrium equation is written around the load-point:

$$\frac{Ps}{4} = \int_0^D \sigma bx \, dx \qquad\qquad 2.16$$

Then the stress σ can be replaced by the cohesive stress, so σ = f(w), and replacing x by a function of w result in:

$$P = \frac{b}{s\theta^s} \int_0^{w_T} f(w)w \, dw \qquad\qquad 2.17$$

In this equation w_T is the opening at the initial notch tip. For large rotation, it can be assumed that $w_T > w_c$, therefore the integral equals to the first order moment of

the softening curve. This also corresponds to, the abscissa $w_G(\overline{W})$ of the center of gravity of the area defined by the curve and the axes, multiply by this area, which is also the same as G_F. Also, θ can be written as u/(s/2), which finally leads to the equation below:

$$P = \frac{bs}{4u^2} \, G_F W_G \qquad\qquad \textbf{2.18}$$

Now, if $P_0= 0$ and $u_A= 0$ due to perfect weight compensation, based on equations 2.12 and 2.18, the value for the center of gravity of the softening curve can be calculated as below:

$$W_G = \frac{4A}{bsG_F} \qquad\qquad \textbf{2.19}$$

Now, it is an easy geometrical problem to totally plot the bilinear softening curve by having f'_t, w_1, G_F, and w_G. So, first the non-dimensional parameters, specified by hats, are defined as below:

$$\hat{\sigma} = \frac{\sigma}{f'_t} \qquad\qquad \hat{w} = \frac{w}{w_{ch}} \qquad\qquad \textbf{2.20}$$

Then, the quadratic equation below should be solved to calculate $\hat{w}_c$:

$$\hat{w}_c^2 - 2\hat{w}_c \frac{3\hat{w}_G - \hat{w}_1}{2-\hat{w}_1} + 2\hat{w}_1 \frac{3\hat{w}_G - 2}{2-\hat{w}_1} = 0 \qquad\qquad \textbf{2.21}$$

The coordinated of kink point are defined as:

$$\hat{w}_k = \hat{w}_1 \frac{\hat{w}_c - 2}{\hat{w}_c - \hat{w}_1} \qquad\qquad \hat{\sigma} = \frac{2-\hat{w}_1}{\hat{w}_c - \hat{w}_1} \qquad\qquad \textbf{2.22}$$
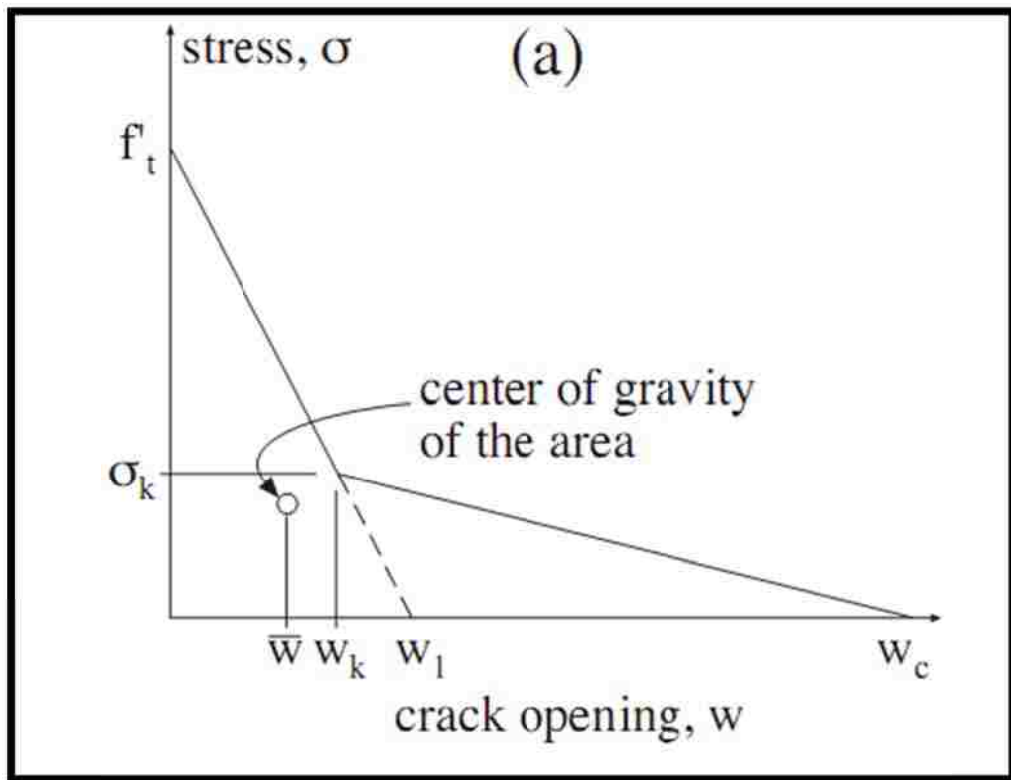
Figure 2.15: (a) Geometry of the bilinear softening curve [39**]**

CHAPTER 3

3 EXPERIMENTAL METHODS

3.1 Test Mix Design for Ultra High Performance Concrete

Currently, there is no international code for constructing UHPC, thus different methods can be used to get proper mix designs with desirable properties. In this paper, the mix design used is based on the work done by Dr. Taha on UHPC at the University of New Mexico [41], and also the report from Federal Highway Administration which characterizes the material behavior of UHPC [42]. The largest granular particle is Calcined Bauxite with average diameter of 3 to 7 mm, the second largest particle is Cement with roughly 15μm average diameter. Silica Fume is the smallest particle with the diameter small enough to fill the voids between cement and calcined bauxite. The materials used in 1 cubic meter are shown below:

Table 3.1: Typical UHPC composition

Material	
Type I/II Cement (kg)	992.3
Silica Fume (kg)	198.5
Calcined Bauxite Fine Aggregate (kg)	1123
Water (L)	223
Glenium 3030 NS (mL)	24800
Rheomac VMA 362 (mL)	5700

This mix can be divided into two parts- solids, and liquids. The solid consists of all the cementitious, aggregate, and filler material. The liquids that were mixed with solid included viscosity modifying admixture (VMA) and a high-range water reducing admixture (HRWA). The viscosity modifying admixture used in this study was Rheomac VMA 362, which increases resistance to segregation and facilitates placement and consolidation, and the Glenium 3030NS as HRWA. Glenium 3030NS reduces water content for a given slump, dosage flexibility for normal, mid and high-range water reduction, produces cohesive and non-segregating concrete mixture, increases compressive and flexural strength at all ages, provides faster setting times and strength development, and enhances finishability and pumpability.

First, all the cement, calcined bauxite, and silica fume were added in the shear mixer and mixed for 2 minutes. Then, half of the water, half of the Glenium, and all of the Rheomac VMA were added. After a wait of 3-5 minutes, the rest of water and Glenium were added to the mix until the mix turned into UHPC with good workability.

3.1.1 Batching, and Curing of UHPC

Due to limited capacity of the mixer, and the large volume of UHPC needed, concrete was cast in 3 different batches. The same mix design was used for all 3

batches. Prior to casting, all the forms for beams and cylinders were oiled. As soon as mixing was completed, the casting of specimens commenced. For each batch after casting, depending on the size of the specimens, the specimens were compacted based on the ASTM standard C192 (ASTM 2006). The compression test cylinder samples were both compacted and vibrated for thirty seconds on the vibration table.

Figure 3.1: The oiled forms and other necessary tools

Figure 3.2: The final mix exiting the mixer

When filing and vibrating of the specimens were done, the specimens were screed. Although screeding is not suggested for UHPC because it's very hard for a large scale batch of concrete, it was implemented here to make the later preparation of the specimens for tests easier. The exposed surface of the specimens was covered in plastics to avoid moisture loss after the screeding. Finally, the specimens were set undisturbed until the demolding. The specimens were demolded approximately 24 hours after casting.

.

Figure 3.3: The specimens after the screeding

The curing treatment applied to concrete is always important, and it is even more

important in the case of UHPC. Hence, after demolding the specimens heat

treatment was used to cure them. All the specimens were submerged in the

controlled temperature water tank with temperature of 50°C. After 28 days, the

specimens were taken to AMEC Earth and Environmental to be grinded and to

obtain the compression tests according to ASTM standard C873 (ASTM 2006).

Split tension tests were also performed at that location according to ASTM

standard C496 (ASTM 2006).

Figure 3.4: The UHPC specimen after the compression test

Figure 3.5: The UHPC specimen after the split tension test

The tables below show the summary of different batches and related test results.

Table 3.2: Number of specimens for two different sizes and cylinders

	Number of 22×6×3 in specimens (Smaller Size)	Number of 30×6×6 in specimens (Larger Size)	Number of 8×4 in Cylinders
Batch 1	4	0	9
Batch 2	0	3	9
Batch 3	2	2	9

Table 3.3: Test results for the compressive strength of specimens

B1-28 days				Average(Psi)	Average(MPa)
F_c (Psi)	21210	20788	21800	21266.00	141.77
B2-28 days				Average(Psi)	Average(MPa)
F_c (Psi)	21580	21530	21320	21476.67	143.18
B3-7 days				Average(Psi)	Average(MPa)
F_c (Psi)	21870	21240	21655	21588.33	143.92
B1-7 days				Average(Psi)	Average(MPa)
F_c (Psi)	19580	19910	19630	19706.67	131.38
B3-7 days				Average(Psi)	Average(MPa)
F_c (Psi)	21060	21260	21120	21146.67	140.98

Table 3.4: Test results for the split tension of specimens

B1-28 days				Average(Psi)	Average(MPa)
F_t (Psi)	1043	1154	1087	1094.67	7.30
B2-28 days				Average(Psi)	Average(MPa)
F_t (Psi)	1020	1070	1374	1154.67	7.70
B3-28 days				Average(Psi)	Average(MPa)
F_t (Psi)	1134	1297	1050	1160.33	7.74

3.2   Test Mix Design for High Performance Concrete

The mix was designed based on the ACI guidelines. Therefore, a mix created initially by Dr. Taha, at Civil Engineering Department, University of New Mexico, was developed to be used to cast HPC. The mix portion for volume of 1 cubic meter is as follows:

Table 3.5: Typical HPC composition

Material	
Type I/II Cement (kg)	302
Fly Ash(kg)	120
Sam Sanders Fine Aggregate (kg)	1290
Sam Sanders Intermediate Aggregate (kg)	635
Water (L)	120
Glenium 3030 NS (Super plasticizer) (mL)	7650
Rheomac VMA 362 (mL)	4140

3.2.1 Batching, and Curing

The HPC was cast in two different sizes just like UHPC, with only one difference that the casting was done in a single batch in a normal mixer unlike UHPC which needed shear mixer.

All the forms for the beams, and cylinders were oiled before beginning of casting. All the aggregates, cement, and fly ash were then added in the mixer, and mixed. Then half of water, Rheomac, and Glenium were added, and mixed for 2-4 minutes. Finally, rest of the water was added to the mix to get the desirable mix which was also workable, and facilitated the casting. Each specimen was compacted according to ASTM standard C192 (ASTM 2006) during the casting. When all the forms were filled up with concrete, the exposed surfaces of the specimens were screeded to facilitate future preparation of the specimens. The specimens were then covered in plastic to avoid any moisture loss, and left undisturbed for 24 hours until demolding. The specimens were demolded approximately 24 hours after casting, and immediately taken to the curing room.

After 28 days, compressive strength test, and split tension test according to C873 (ASTM 2006), and ASTM standard C496 (ASTM 2006) respectively, were performed, the average results for three specimens are as below:

Table 3.6: Compressive test results of the specimens

28 days				Average(Psi)	Average(MPa)
F_c (Psi)	8264	8434	8185	8294.33	55.30

Table 3.7: Tensile test results of the specimens

28 days				Average(Psi)	Average(MPa)
F_t **(Psi)**	656	720	694	690.00	4.60

3.3   ACI Committee 446: Fracture Toughness Testing of Concrete

3.3.1   Summary of Test Method

In this test method, notched beams for two different sized of UHPC and HPC were tested to help determine the parameters of various models of concrete fracture. Center-loaded notched concrete beams were tested under closed loop CMOD control (with compensation for specimen self-weight). The relationship between load, load point displacement, LPD, crack mouth opening displacement, CMOD, versus time, t were recorded and reported.

3.3.2   Specimens

ACI committee 446 has determined several provisions that should be met when the concrete specimens are cast [**37**]:

- "The geometry and manufacture of the specimens in this procedure shall conform to the general provisions of Practices C 31 (field specimens) or C 192 (laboratory specimens) applicable to beam and prism specimens."

- "A minimum of three beam specimens shall be cast. Whenever practical, all the specimens shall be cast from the same concrete batch."
- "The beam specimens shall be prismatic beams of rectangular cross section with a sawn central notch."
- "Beam depth, D, shall be at least 6 times greater than the maximum aggregate size, d_a ($D \geq 6d_a$). The preferred depth, D, is 150 mm if $d_a \leq 25$ mm."
- "Beam width, B, shall be at least 6 times greater than the maximum aggregate size, da ($B \geq 6d_a$). The preferred width, B, is 150 mm if $d_a \leq 25$ mm."
- "The loading span (S) shall be equal to three times the beam depth (3D), within ±5%."
- "The total length (L) of the specimen shall be at least 50 mm longer than three times the beam depth ($L \geq 3D + 50$ mm)."
- "The nominal notch depth (a_0) shall be equal D/3, to within ±10%. Deviations up to 10% of the nominal value may be accepted for a whole test series ($0.30 \leq a_0/D \leq 0.37$). But, within a series, notch depths of individual specimens shall not deviate from the mean by more than 2%."
- "The notch width (N) shall be no larger than the 2% of the beam depth ($N \leq 0.02D$)."
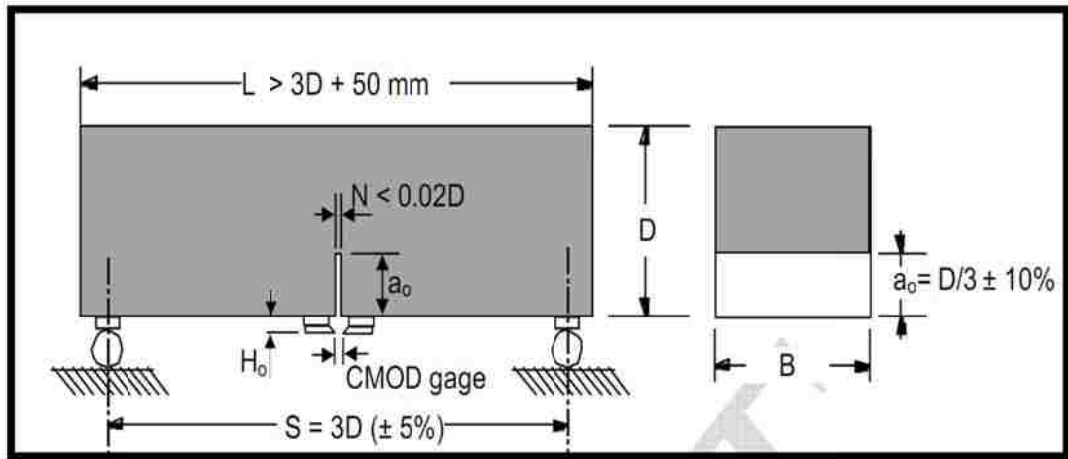
Figure 3.6: Specimen geometry and dimensions [37**]**

All of the above conditions were met. Due to limited capacity of shear mixer, and the amount of concrete needed, the concrete casting was divided into three different batches, and the specimens were all cast according to ACI Committee 446 regulations. The specimens were cast in two different beam sizes:

Table 3.8: Details of two different beam sizes for UHPC

	Smaller Size	Larger Size
D (mm)	76.2	152.4
B(mm)	152.4	152.4
N(mm)	3.048	3.048
a_0(mm)	25.4	50.8
S(mm)	228.6	457.2
L(mm)	558.8	762
Total number of beam Specimens	6	5

Table 3.9: Details of two different beam sizes for HPC

	Smaller Size	Larger Size
D (mm)	76.2	152.4
B(mm)	152.4	152.4
N(mm)	3.048	3.048
a_0(mm)	25.4	50.8
S(mm)	228.6	457.2
L(mm)	558.8	762
Total number of beam Specimens	6	6

3.3.3 Apparatus

ACI committee 446 considered some provisions for testing machine for beam specimens [**37**] :

- "A servo-hydraulic or electromechanical testing machine shall be used that provides closed-loop control with the crack mouth opening displacement (CMOD) as the feedback signal. Sufficiently high machine stiffness is required to prevent CMOD snap-back instability."
- "The load cell installed on the machine for these specific tests shall give load readings accurate to within 1% of the recorded peak load."
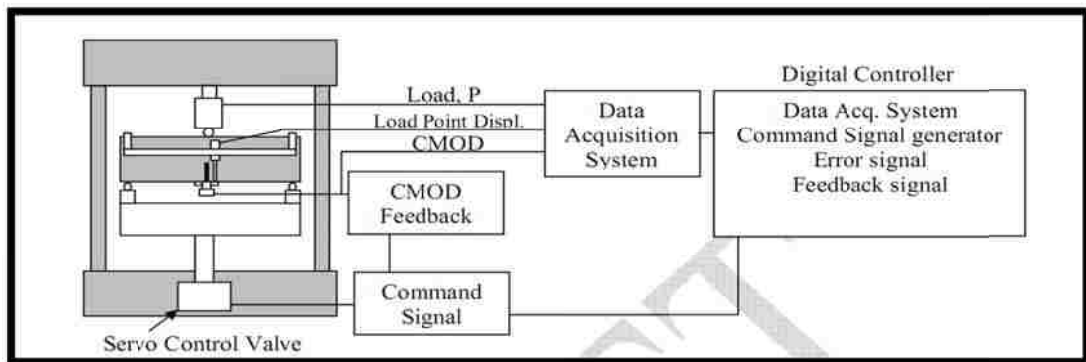
Figure 3.7: Schematic representation of the control system for a closed loop set up [37]

The MTS Bionix machine in the structural laboratory of civil engineering department was used, which satisfied all the conditions above.

Figure 3.8: The MTS Bionix machine

ACI Committee 446 has determined the following conditions for loading

apparatus for beam specimens [**37**]:

- "The loading apparatus (Figure 3.10) for the bending tests shall provide
  two supports and a central loading block suitably mounted to minimize
  eccentricities (torsion), to keep the loading span within the specified
  tolerances, and to minimize friction at the supports."
- "The loading block (Figure 3.10) shall be cylindrical with a circular
  boundary of a radius $0.1\ D \leq R \leq 0.2\ D$ and a length equal or exceeding
  the specimen width, B. It shall be able to rotate about the longitudinal axis
  up to $\pm 10^{o}$ to accommodate small specimen imperfections without
  introducing torsion. The loading block shall be suspended from the load
  cell (by means of springs, e.g.) so that the load cell, and not the specimen,
  directly holds the loading block's weight." For this purpose the loading
  block was suspended from the load cell using rubber bands as its shown
  in figure below:

Figure 3.9: Suspension of loading block from loading cell using rubber bands

- "The supports shall provide essentially friction-free reactions. The resultant friction coefficient shall be less than 0.01. This usually requires rolling contacts. Rolling shall proceed on ground hardened steel surfaces, never on concrete surfaces. If rollers are provided (Figure 3.10) they shall be actually free to roll (never placed into a V-shaped groove). Ground hardened steel plates of suitable size shall be placed between the specimen and the rollers (Figure 3.10). The plates shall have a width of 0.15 to 0.25 of the beam depth (D), and a depth of not less than one-half of the width. Both the plates and the rollers shall have a length exceeding the beam width, B. Other types of supports based on roller or needle bearings may be used if adequately designed for low friction."

- "To minimize torsion, one of the supports shall be free to rotate about an axis parallel to the beam's longitudinal axis (Figure 3.10)."

- "While the rollers can be clamped during the test setup, it is essential to unclamp them before starting the test. It is also essential to keep the rolling surfaces free of any debris that might be produced during handling. For this purpose, the supports were cleaned from any dust after the handling of the specimens and before performing the tests."
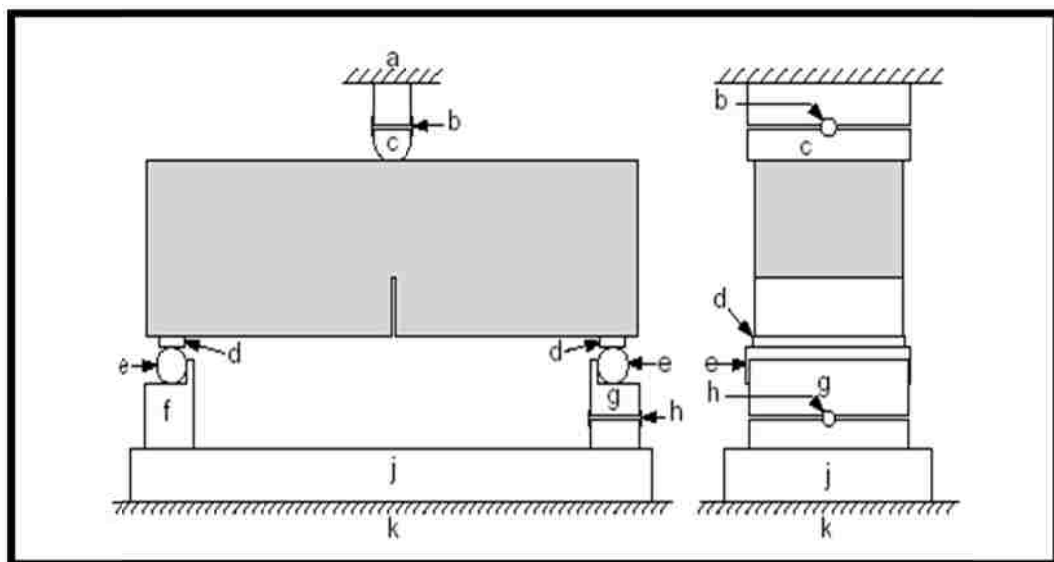
Figure 3.10: Sketch of the loading apparatus((a) load cell; (b) hardened steel shaft; (c) rotating loading block; (d) hardened steel bearing plates; (e) hardened steel rollers; (f) fixed support; (g) rotating support; (h) hardened steel shaft; (j) stiff steel beam; (k) machine frame.) [37]

3.3.4 Compensation of Specimen Self-Weight

ACI Committee 446, unlike the methods recommended by RILEM, has provided some provisions for compensation of self-weight to avoid unstable failure before the end of the test due to the self-weight of the specimens.

- "Weight compensation shall be provided using either counterweights at each end of the specimen, as sketched in Figure 3.11 and illustrated in Figure 3.11, or the counterweights may consist of the projecting ends of the concrete beam as sketched in Figure 3.11."

- "The beam length, L, or counterweights shall be chosen to ensure a hogging bending moment at mid-span, M, such that $mgS/32 < M < mgS/16$." In this equation m is the beam mass, g is the acceleration due to gravity, and S is the span.
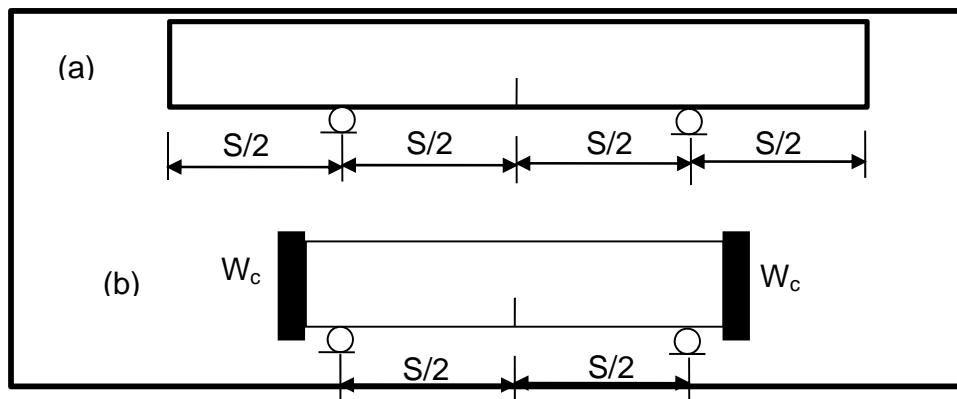
Figure 3.11: Weight compensation: (a) double-length specimen; (b) attached counter-weights [37]

For smaller size of beams (558.8*152.4*76.2 mm), the projecting ends of the beams were used as the counterweights on two sides of the beams, which also satisfied the above criterion for hogging bending moment at mid-span as follows:
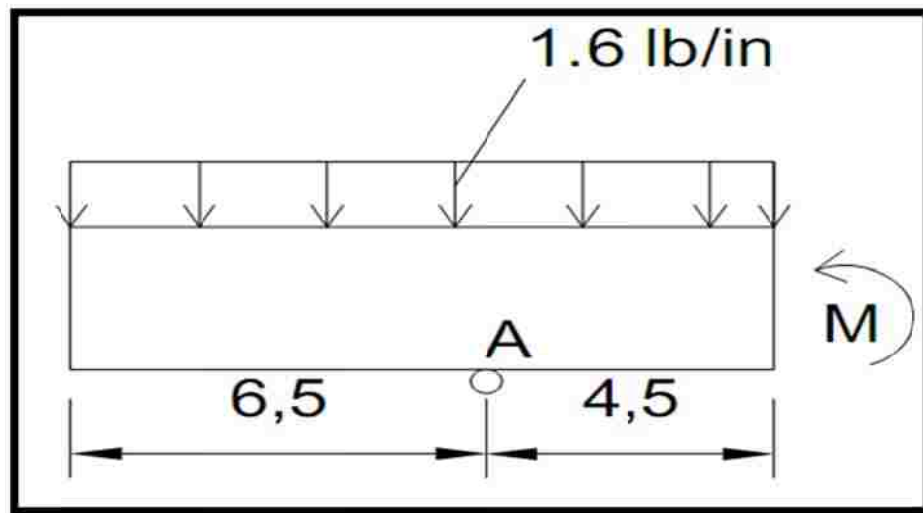
Figure 3.12: Details for half of the beam (Beam dimensions are in inch)

$$W = \frac{35.2}{22} = 1.6 \frac{lb}{in}$$

$$1.6 \times 11 \times 1 + M = 0 \ \rightarrow M = -17.6 \ lb.in = -1993.4 \ N.mm$$

Table 3.10: Hogging bending moment boundaries

m (kg)	16
S(mm)	228.6
mgS/32 (N.mm)	1121.28
mgS/16 (N.mm)	2242.57

Thus;

1121.28 < 1993.4 < 2242.57 ➜ No Counterweights needed

For the larger size of beams (762*152.4*152.4mm), in order to meet the above provisions, the counterweights were attached to the both ends of the beam (Figure 3.13):

Figure 3.13: Counterweights details for the larger size of beams

The attached counterweights were 4.5 kg on each side. The two values for boundaries of hogging bending moment were calculated as below:

Table 3.11: Hogging bending moment boundaries

m (kg)	46
S(mm)	457.2
mgS/32 (N.mm)	6447.38
mgS/16 (N.mm)	12894.75

The hogging moment assuming P= 10 lb for counterweights and details below is calculated:
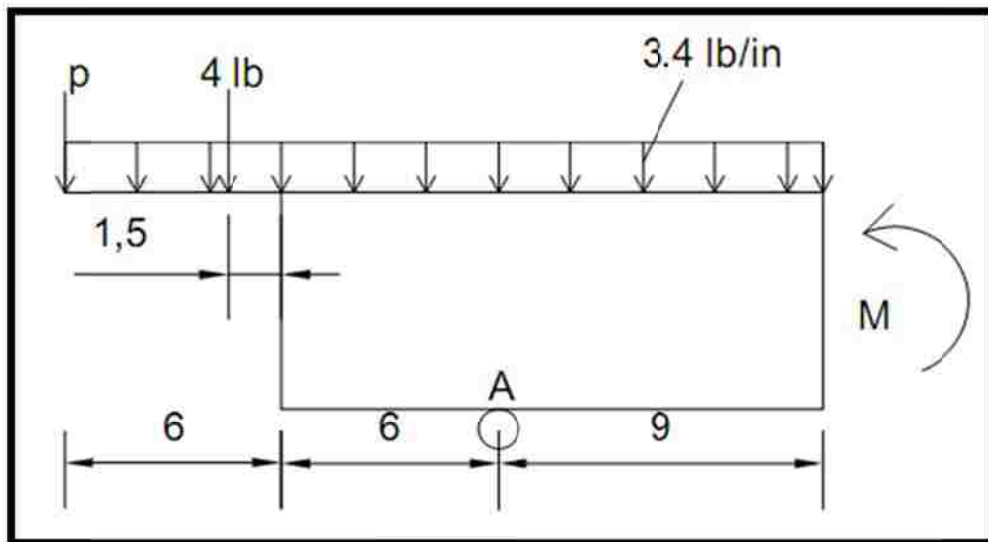
Figure 3.14: Details for half of the beam (Beam dimensions are in inch)

4 lb is due to the weight of the cantilever which is showed in Figure 3.13

Calculating the moment about point A:

$$W = \frac{101.2}{30} = 3.4 \frac{lb}{in}$$

$$10(12) + 4(7.5) - 3.4 \times 15 \times 1.5 + M = 0 \rightarrow M = -73.5 \, lb.in = -8324.7 \, N.mm$$

Thus,

6447.38< 8324.7< 12894.75 ➔ the assumption for P was correct.

It should be noted that while the above calculation was done for UHPC, it is also applicable to HPC, since the weight of the specimen for two different concrete is almost the same, and the beam dimension and test setup are identical.

3.3.5 CMOD and LVDT

ACI Committee 446 has determined the following conditions for the extensometer for measuring the CMOD [37]:

- "The CMOD shall be measured with a clip-on gage or similar extensometer (Figure 3.15) giving readings accurate within 5 µm (five micron) over a range of 0.0133D."
- "The gage length of the extensometer shall be centered on the notch; the gage length shall be less than $0.25a_0$ (Figure 3.15)."
- "The fastenings of the knife edges to the specimen shall be within $0.25a_0$ of the notch center line (Figure 3.15) (If the knife edges are glued to the specimen surface, all the glued zone shall be within $0.25a_0$ of the notch center line)."
- "The distance H_0 of the extension line to the specimen surface shall be as small as possible, and never greater than $0.1a_0$ (Figure 3.15)."
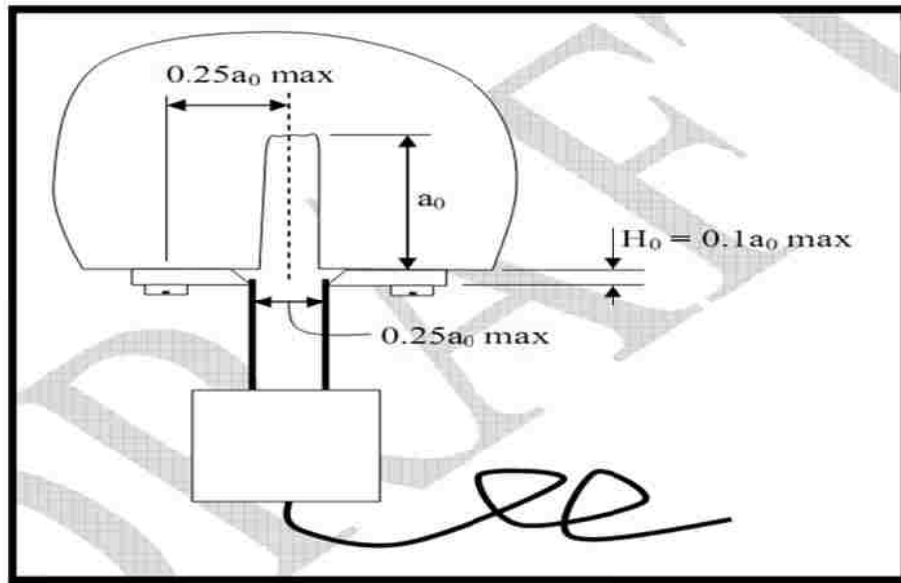
Figure 3.15: Detail of clip gage and knife-edges [37]

In the present tests, the knives were glued to the concrete specimen by super glue for both sizes, and the value for H_0 was 1.5748 mm which is less than 2.54 mm.

The clip gages were from MTS with Model number: 632.02E-20, the maximum compressed length was 0.2 in, and the range of travel was +0.1/-0.05 in. To be able to use the clip gages properly, they were calibrated initially with micrometer and with aid of the software for the MTS machine. This resulted in readings accurate within 5 μm (five micron).
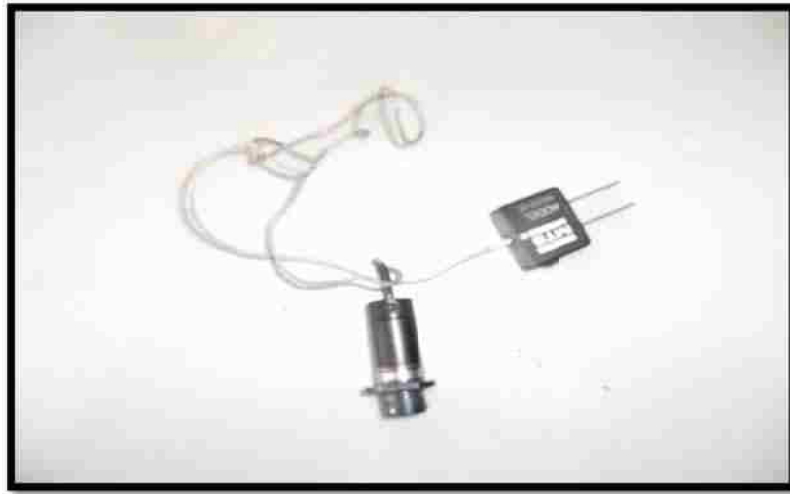
Figure 3.16: MTS clip gage

ACI Committee 446 has determined the following for measuring the load point displacement [**37**]:

- "To avoid measuring the inelastic deformation associated with the supports, the LPD shall be determined relative to the points directly above the support points and below the loading point by means of a reference frame (Figure 3.17)."

- "For this method to give accurate results, the reference frame for measuring the displacement shall be sufficiently stiff. A maximum reference frame deflection under self-weight of 2 μm (two microns) is allowed."

- "The reference frame shall be supported by three conically tipped screws, two over one support and one centered on the other support (Figure 3.17)."

- "Two LVDTs, whose readings shall be accurate within 10 µm (ten microns) over a range of 0.01D, shall be used to read the vertical deflection. The LVDTs shall be symmetrically located on the central cross-section plane, one on each side of the specimen. The LPD signal (δ) shall be computed as the average of the measured signal from both LVDTs."

- "The LVDTs shall be rigidly fastened to the reference frame with their moving tips lying on a plate fastened to one of the two halves of the specimen (Figure 3.17). A reasonably simple solution is to provide two plates as shown in (Figure 3.17) that contain the knife edges to fasten the CMOD gage. One of them (on the right in the figure) extends outside the specimen width and has two wings protruding through the notch plane, thus providing a support surface for the moving tips of the displacement transducers."
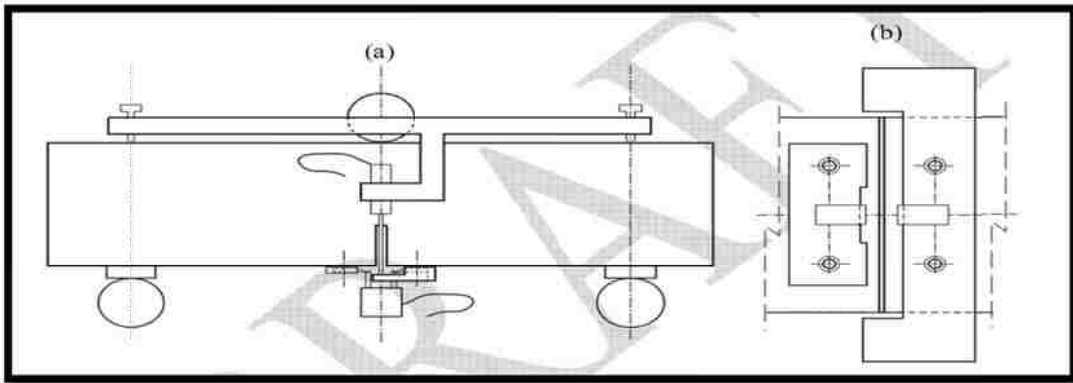
Figure 3.17: Measurement of load-point displacement. (a) Reference frame for displacements, LVDT, bottom reference plate and CMOD gage. (b) Sketch of bottom view of specimen with reference plate [37]

To meet the above conditions, two different frames were used for each size of beam. One of the frames was already built and available in the lab, and another frame for smaller size of beams was built in the mechanic shop in the University of New Mexico.

Figure 3.18: Frame for the smaller size of beams

The LVDTs were form Schaevitz Company with model number: 250 MHR-0396 and the range was ± 0.25 in. To be able to use the LVDTs properly, they were calibrated initially with micrometer and aid of the software for the MTS machine, which resulted in readings accurate within 10 µm (ten microns).

Figure 3.19: Schaevitz LVDT

Figure 3.20: View of the specimen, with the CMOD gage in the center, and the mounting plates with wings to provide support for the mobile tips of the displacement transducers

67

3.3.6 Beam Specimen Preparation

The beams were taken out of the tank one day before the test, and were notched using a diamond saw with water cooling system. The pressure of the saw was kept as low as possible to avoid any likely damage to the concrete. Also the circular saw caused the notch front to be perpendicular to the planes, which were horizontal during the casting. Then, the specimens were handled very carefully to avoid any damages.

The beams were removed again out of the tank with enough caution to avoid any damages since they were already notched, and the support lines and center line for loading were immediately marked. Meanwhile, the specimen was kept wet by using water sprayed on the specimen, so the dry surface was totally avoided during the beam preparation.

It was verified that the load bearing areas are even using a ground steel rod and a leaf type feeler gage of 0.2 mm. The gaps larger than 0.2 mm were detected and removed by grinding that area.

The knives were attached to the specimen along the crack using super glue.

Figure 3.21: The attachment of knives to specimen with the super glue, and keeping of the specimen wet by water spray

3.3.7 Beam Test

The beam was gently placed on the loading device, while the roller supports were fixed to facilitate the placement. The beam was then centered very carefully so that the notch was placed in the mid position within 1 mm. Meanwhile, the beam was still kept wet by water spray.

Figure 3.22: Attachment of clip gages to the knives

The clip gages were placed between the knives, and the initial values for CMOD were adjusted to be close to zero.

In the next step the frame was placed on the beam, and the counterweights were added for the larger size of beams (No counterweights needed for the smaller size of beams). Afterwards, the LVDTs were placed in the holes in the frame, and then the core for LVDTs was added to be on top of the knives.

Figure 3.23: Placement of LVDTs in the frame

The load channel was set to zero and the specimen was slowly pre-loaded to 5 to 10 percent of estimated maximum peak load, which was approximated simply by the maximum tensile strength of the material, and assuming that the effective area is above the crack. If the estimated pre-load exceeds 15 percent of the peak load, the test is not acceptable, and it should be repeated. Finally, it was reassured that there was no debris or dust on the rollers, and that they were unclamped.

Figure 3.24: The final beam setup for starting the test

3.3.8 Loading of the Beam

ACI committee 446 has recommended that, the test should be done in monotonically increasing CMOD mode. The loading rate should be adjusted such that the maximum load is reached in 3 to 5 minutes; then the rate should be kept constant till the load decreases to 33 percent of the peak load. The CMOD rate is then increased up to ten times the initial rate and should be kept constant till the end of the test. The test is valid only if it is completed in 30 minutes.

If the test is done under constant rate of CMOD increase, it might take 3 to 5 hours. The solution given above is an expedient. The ACI committee 446

proposed that, if the machine can be given any specified evolution of CMOD vs. time, a good choice could be to use the piecewise function defined as

$$CMOD = w_0\ t/t_0 \qquad \text{for } t < t_0,$$

$$CMOD = w_0\ \exp[(t-t_0)/t_0], \text{ for } t > t_0$$

3.1

Where $t_0 = 3\text{-}5$ min is the (nominal) time to peak and w_0 the (nominal) CMOD at the peak.

By using the above equation, the completion of the test should be achieved in approximately 5 times the time to the peak load (i.e. between 15 and 25 minutes, which is reasonable). The value for w_0 has to be initially guessed and then corrected from the results of a trial test, just as for the initial rate.

Some dummy specimens were tested to obtain a good loading rate which could satisfy the above conditions. The MTS procedure editor was used to input the loading rate for CMOD control mode. The program divided the loading to different time intervals with an assigned value for CMOD at the end of each time interval. The dummy tests showed that, since ultra-high performance concrete is very brittle, the CMOD increase rate should be very slow to avoid any sudden or unstable failure of the specimen, and to be able to get a good softening curve. Based on the dummy tests, the values for W_0 and the CMOD increase rate were reevaluated, and the loading program was finalized.

Figure 3.25: End of test

The same procedure was also used for HPC, with only one difference that, since HPC is not as brittle as UHPC, the rate of CMOD increase can be a little faster. However, the proper rate for CMOD increase was determined by trial and error based on the results for the tests of the dummy specimens.

Immediately after completion of the tests, the specimens and all the rubbles, which were scabbed of the specimen halves were weighted on the scale with precision of 0.1 kg.

All dimensions were measured to the nearest 0.01 mm, including the beam depth

(D) at the central cross section at the two surfaces of each half of the specimen,

the notch depth (a_0) at the central cross section at the two surfaces of each half

of the specimen, and the beam width (B) at the front of the notch and at the top

of the. Finally the average of the measured values was used to run the analysis.

3.3.9 Challenges in the Loading Procedure

The loading procedure proposed by ACI Committee 446 has not considered the

influence of concrete strength on the loading pattern. Therefore, it was

cumbersome to determine a good loading pattern. Initially, stroke control mode

was used to investigate the feasibility of obtaining a good softening curve with no

unstable fracture for the smaller size of HPC. The results for the dummy

specimens revealed the inapplicability of the stroke control mode. A sudden

decrease in the load was inevitable in the stroke control which prevents obtaining

a good softening curve as shown in Figure 3.26.
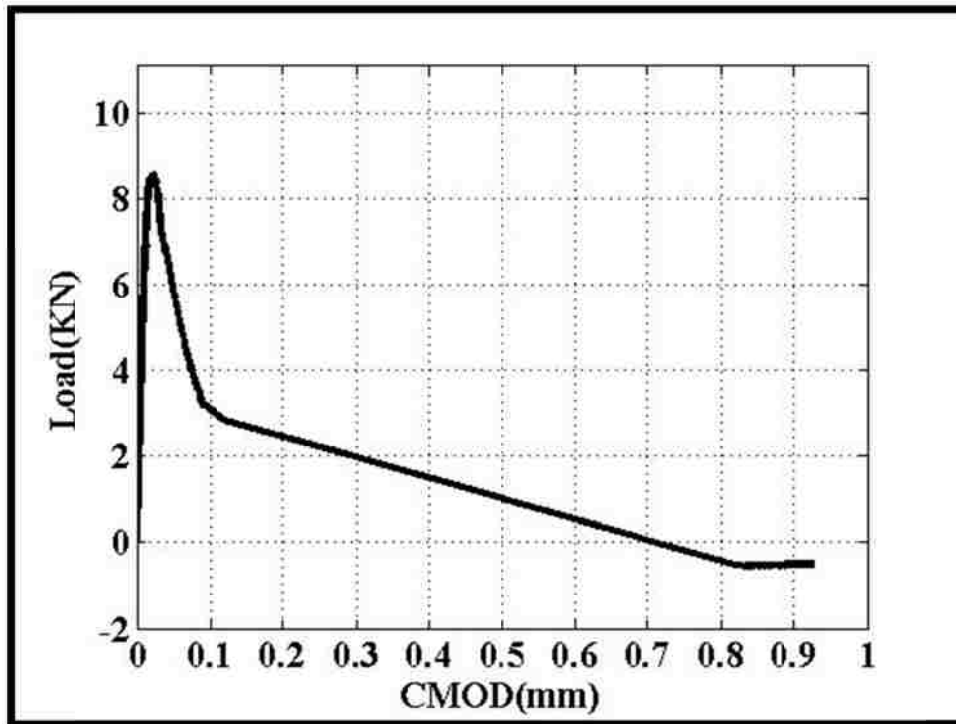
Figure 3.26: Load versus COMD for the smaller size of HPC using stroke control mode

Thus, all the remaining specimens were loaded in CMOD control mode. The CMOD increase rate was set to be very slow for UHPC to obtain a good softening curve which also avoided any instability at the end of the test. Hence, the loading procedure mentioned in ACI Committee 446 needs a thorough revision to be applied to more brittle concrete like UHPC. Moreover, it was observed that, if the time for completion of the test can exceed 30 minutes, a better softening behavior can be obtained for UHPC.

Table 3.12: Summary of post-test measurements for UHPC, smaller size

	558.8*152.4*76.2 mm					
Specimen name	B3-S1	B3-S2	B1-S1	B1-S2	B1-S3	B1-S4
Preload(N)	743	610	610	735	753	764
Weight(KG)	17.2	17.2	17.2	17.05	16.5	16.55
Dimensions						
D_1(mm)	75.46	77.09	77.09	78.44	76.49	75.36
D_2(mm)	76.05	77.25	77.25	78.05	75.11	74.51
D_3(mm)	75.56	76.58	76.58	78.54	75.58	74.4
D_4(mm)	76.33	77.19	77.19	78.26	76.32	75.49
D_{ave}	75.85	77.03	77.028	78.323	75.875	74.94
B_1(mm)	153.5	153.3	153.25	153.62	153.31	153.39
B_2(mm)	153.3	154	153.97	154.29	154.79	154.76
B_3(mm)	154.1	153.3	153.3	154.24	153.05	154.04
B_4(mm)	153.8	153.5	153.47	153.89	153.75	154.77
B_{ave}	153.6	153.5	153.5	154.01	153.73	154.24
a_1(mm)	23.12	27.26	27.26	27	23.58	23.63
a_2(mm)	27.96	24.66	24.66	31.73	24.31	25.67
a_3(mm)	27.81	27.38	27.38	31.49	24.11	26.94
a_4(mm)	23.67	24.35	24.35	27.43	24.13	23.6
a_{ave}	25.64	25.91	25.913	29.413	24.033	24.96

Table 3.13: Summary of post-test measurements for UHPC, larger size

	762*152.4*152.4 mm				
Specimen name	B3-S3	B3-S4	B2-S1	B2-S2	B2-S3
Preload(N)	1206	1103	1156	1102	1196
Weight(KG)	46.05	45.8	45.95	45.6	45.8
Dimensions					
D_1(mm)	151.31	153.38	154.49	152.82	152.63
D_2(mm)	153.08	151.94	153.28	152.97	152.56
D_3(mm)	151.25	154.29	153.43	153.34	151.88
D_4(mm)	153.52	152.12	155.63	152.65	153.28
D_{ave}	152.29	152.93	154.11	152.95	152.59
B_1(mm)	153.25	150.66	151.03	153.13	153.1
B_2(mm)	153.01	151.4	151.2	153.52	153.21
B_3(mm)	152.58	151.04	152.01	153.56	153.08
B_4(mm)	152.97	151.42	151.2	153.15	153.36
B_{ave}	152.95	151.13	151.36	153.34	153.19
a_1(mm)	49.3	56.57	49.7	50.03	48.22
a_2(mm)	55.9	56.17	48.93	48.97	49.48
a_3(mm)	51.87	55.53	49	48.62	47.88
a_4(mm)	57.61	56.37	49.33	48.9	49
a_{ave}	53.67	56.16	49.24	49.13	48.65

Table 3.14: Summary of post-test measurements for HPC, smaller size

	558.8*152.4*76.2 mm		
Specimen Name	S1	S2	S3
Preload(N)	365	534	447
Weight(KG)	15.9	15.15	15.8
Dimensions			
D_1(mm)	79.69	75.2	78.81
D_2(mm)	81.57	76.73	78.64
D_3(mm)	83.03	75.5	78.54
D_4(mm)	81.53	75.25	78.65
D_{ave}	81.455	75.67	78.66
B_1(mm)	154.53	156.25	155.61
B_2(mm)	154.84	154.96	154.69
B_3(mm)	154.42	155.94	155.61
B_4(mm)	155.41	154.88	155.3
B_{ave}	154.8	155.5075	155.3025
a_1(mm)	26.39	26.49	26.07
a_2(mm)	25.3	26.63	26.12
a_3(mm)	26.42	26.36	26.08
a_4(mm)	25.13	27.88	25.29
a_{ave}	25.81	26.84	25.89

79

Table 3.15: Summary of post-test measurements for HPC, larger size

	762*152.4*152.4 mm					
Specimen Name	**S1**	**S2**	**S3**	**S4**	**S5**	**S6**
Preload(N)	679	733	729	828	631	861
Weight(KG)	42.65	42	41.6	42.1	41.7	41.2
Dimensions						
D_1(mm)	151.71	153.3	153.37	153.48	151.73	152.53
D_2(mm)	151.18	153.59	154.84	153.13	154.33	151.64
D_3(mm)	150.2	153.21	153.82	154.02	154.89	151.67
D_4(mm)	151.42	153.83	153.43	153.5	152.73	152.62
D_{ave}	151.1275	153.4825	153.865	153.5325	153.42	152.115
B_1(mm)	154.88	152.12	154.4	157.43	152.49	152.18
B_2(mm)	158.34	155.26	156.84	161.06	152.74	150.57
B_3(mm)	154.84	153.75	157.21	155.91	153.11	152.98
B_4(mm)	158.63	156.39	153.31	159.04	153.21	151.09
B_{ave}	156.6725	154.38	155.44	158.36	152.8875	151.705
a_1(mm)	47.81	51.98	51.28	49.67	45.38	48.42
a_2(mm)	50.7	54.11	50.47	50.67	51.8	53.72
a_3(mm)	49.69	54.19	50.16	50.19	51.56	52.46
a_4(mm)	48.18	52.92	49.89	50.65	46.96	48.36
a_{ave}	49.095	53.3	50.45	50.295	48.925	50.74

CHAPTER 4

4 EXPERIMENTAL RESULTS AND DISCUSSION

4.1 Test Results Using ACI Committee 446 Equations

ACI Committee 446 equations will be used to obtain the fracture parameters for two different sizes for both UHPC and HPC [**37**]. The basic concepts behind these equations were already discussed in the literature review.

4.1.1 Modulus of Elasticity

In the first step, the initial compliance C_i was evaluated by fitting a straight line to the segment of load-CMOD curve with measured loads between 15% and 55% of the peak load.

$$C_i = \frac{\Delta(CMOD)}{\Delta P'}$$

4.1

C_i = initial compliance, µm N^{-1}.

Δ (CMOD) = variation of CMOD, µm.

$\Delta P'$ = variation of measured load, N.

Later, this initial compliance is used to calculate the Young's Modulus of each specimen as follows:

81

$$E = \frac{6Sa_0}{C_i BD^2} V_1(\alpha'_0)$$

Where, $\alpha'_0 = \frac{a_0 + h}{D + h}$

4.2

Where, E is elastic modulus(GPa), C_i is initial compliance(μm N^{-1}), B is beam thickness (mm), D is beam depth (mm.), a_0 is notch length(mm), h is Distance of the knife edges to specimen surface(mm).

And,

$$V_1(\alpha) = 0.8 - 1.7\alpha + 2.4\alpha^2 + \frac{0.66}{(1-\alpha)^2} + \frac{4D}{S}(-0.04 - 0.58\alpha + 1.47\alpha^2 - 2.04\alpha^3)$$

4.3

4.1.2 Far Tail Constant, A

P'$_R$, the residual load is determined from the last data recorded by load cell, and the corresponding CMOD is denoted as W$_{MR}$. Then, the load was corrected using equation below:

P$_1$ = P' − P'$_R$

4.4

The curve for corrected peak load, P$_1$ versus CMOD was plotted, and then W$_{MA}$, the intersection of the rising part of the curve with the CMOD axis was determined. For the points in the record past the peak for which the corrected

load is less than or equal to 5% of the corrected peak load, the quantity X was calculated as follows:

$$X = \left(\frac{4D}{S}\right)^2 \left| \frac{1}{\left(w_M - w_{MA}\right)^2} - \frac{1}{\left(w_{MR} - w_{MA}\right)^2} \right|$$

4.5

Where

W_M = recorded CMOD, mm.

W_{MR} = CMOD at the end of test, mm.

W_{MA} = CMOD at zero P_1 for the rising part of curve, mm.

After the values for X are calculated, the curve of P_1 versus X is plotted, and the least square method was used to fit a quadratic equation to the curve.

P1 = X (A+KX**)**

4.6

Constant, A will be evaluated in N-mm^2 with three significant digits (K is not needed).
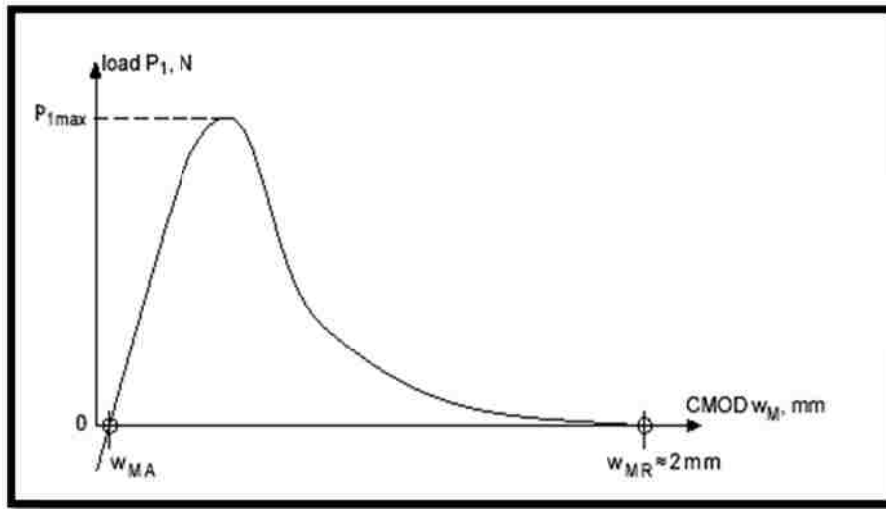
Figure 4.1: Plot of corrected load P_1 versus CMOD [37]

The plots for corrected peak load versus CMOD for all the specimens for two sizes for both UHPC and HPC are shown below:
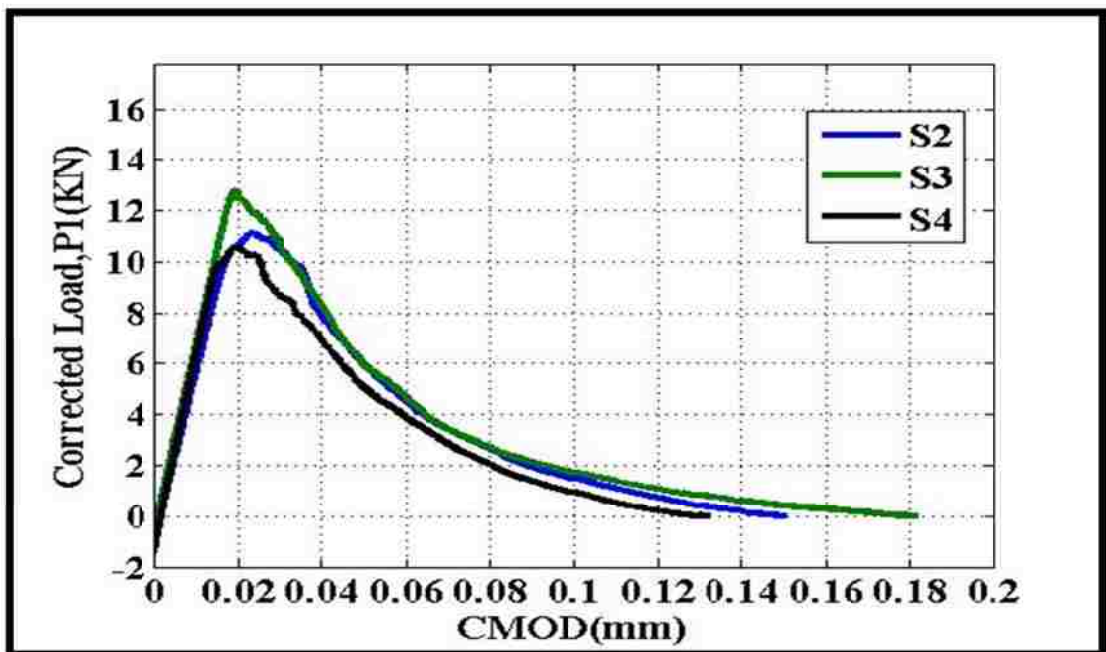
Figure 4.2: Corrected load P_1 versus CMOD for the smaller size of UHPC

84
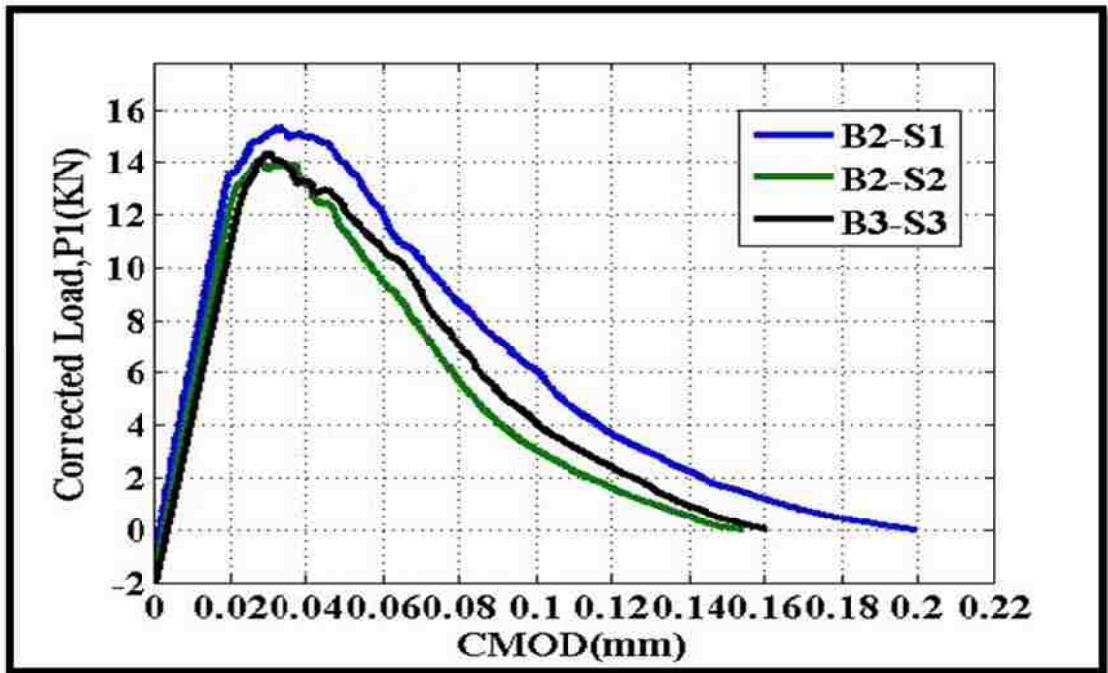
Figure 4.3: Corrected load P$_1$ versus CMOD for the larger size of UHPC
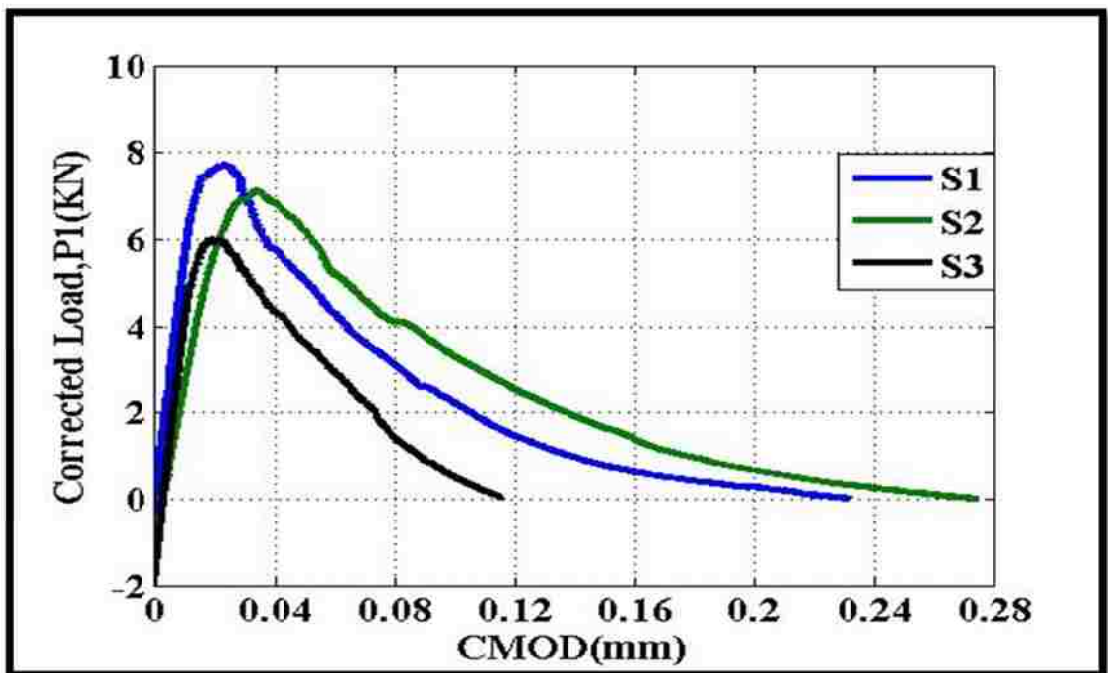
Figure 4.4: Corrected load P$_1$ versus CMOD for the smaller size of HPC

85
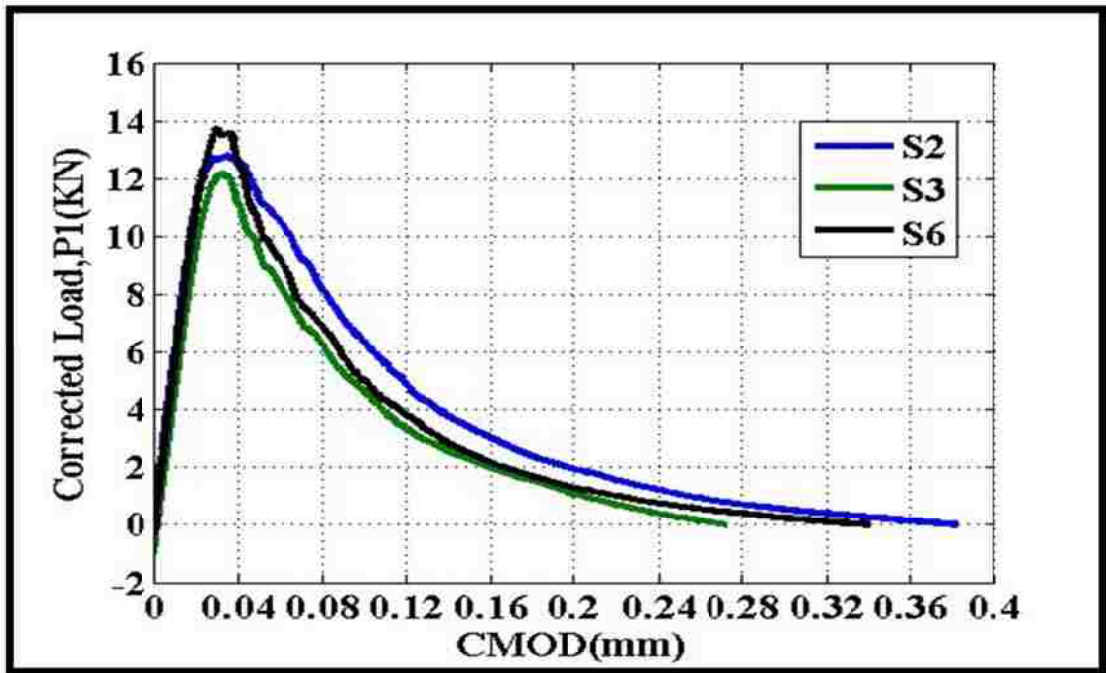
Figure 4.5: Corrected load P_1 versus CMOD for the larger size of HPC

4.1.3 Net Plastic Flexural Strength, f_p

When the brittleness length l_1 is much bigger than the beam depth, the beam exhibits the behavior of rigid-perfectly plastic in tension and rigid in compression. The tensile strength of this ideal material corresponds to plastic stress in tension, f_p which can be calculated by taking moment equilibrium about the center loading point acting on half the specimen when the cross section acts as a fully plastic material [**37**]:
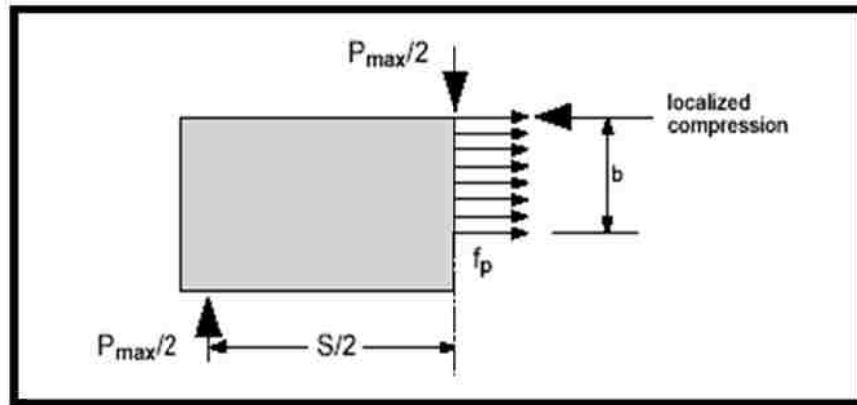
Figure 4.6: Definition of net plastic strength [37**]**

The effective peak load which takes into account the finite length of the tail of the record is initially calculated as below:

$$P_{\max} = P_{1\max} + \frac{A}{\left(w_{MR} - w_{MA}\right)^2}$$

4.7

Where

$P_{\max}$ = effective peak load, N.

$P_{1\max}$ = corrected peak load, N.

Thus, the net plastic flexural strength of the beam is:

$$f_p = \frac{P_{\max} S}{2Bb^2}$$

4.8

The summary of results from the above equations to calculate modulus of elasticity, net flexural strength, and constant A, is shown below:

Table 4.1: Summary of results for the smaller size of UHPC

Specimen Name	B1-S2	B1-S3	B1-S4	Average	Standard Deviation
E (MPa)	58574.468	49367.287	57021.162	54987.64	4928.94
F_p (MPa)	3.665	3.689	3.257	3.54	0.24
A (N-mm^2)	15.219	18.393	6.870	13.49	5.95

Table 4.2: Summary of results for the larger size of UHPC

Specimen Name	B2-S1	B2-S2	B3-S3	Average	Standard Deviation
E (MPa)	52175.173	49777.511	45610.522	49187.74	3321.83
F_p (MPa)	2.271	2.039	2.178	2.16	0.12
A (N-mm^2)	40.816	14.810	33.979	29.87	13.48

Table 4.3: Summary of results for the smaller size of HPC

Specimen Name	S2	S3	S4	Average	Standard Deviation
E (MPa)	42734.88	43893.64	40802.32	42476.95	1561.72
F_p (MPa)	2.24	2.20	1.97	2.14	0.15
A (N-mm^2)	26.990	28.44	16.968	24.13	6.25

Table 4.4: Summary of results for the larger size of HPC

Specimen Name	S2	S3	S6	Average	Standard Deviation
E (MPa)	43894.36	37199.44	42199.99	41097.93	3480.86
F_p (MPa)	1.97	1.78	2.12	1.96	0.17
A (N-mm^2)	86.213	55.331	56.630	66.06	17.47

4.1.4 Brittleness Length, l_1, and Horizontal Intercept, w_1

ACI Committee 446 has proposed the following equations to calculate the brittleness length and horizontal intercept:

$$l_1 = \kappa D \left[\frac{11.2}{\left(x^2 - 1\right)^2} + \frac{2.365}{x^2} \right]$$

4.9

$\kappa = 1 - \alpha_0^{1.7}$

$\alpha_0 = a_0/D$ = notch-to-depth ratio.

D = beam depth, mm.

a_0 = notch length, mm.

$x = f_t/f_p$ = inverse relative plastic strength.

f_p = net plastic flexural strength, MPa.

f_t = tensile strength, MPa.

Then,

$$w_1 = 1000 \frac{2f_t}{E} l_1$$

4.10

The summary of results from the above equations is shown in the tables below:

Table 4.5: Summary of results for the smaller size of UHPC

Specimen Name	B1-S2	B1-S3	B1-S4	Average	Standard Deviation
l_1 (mm)	88.23	142.2	69.4	99.94	37.79
W_1 (μm)	18.76	27.77	12.54	19.69	7.66

Table 4.6: Summary of results for the larger size of UHPC

Specimen Name	B2-S1	B2-S2	B3-S3	Average	Standard Deviation
l_1 (mm)	46.88	34.73	41.66	41.09	6.09
W_1 (μm)	13.12	10.19	13.33	12.21	1.76

Table 4.7: Summary of results for the smaller size of HPC

Specimen Name	S1	S2	S3	Average	Standard Deviation
l_1 (mm)	109.14	101.43	65.93	92.17	23.05
W_1 (μm)	17.39	19.50	14.87	17.25	2.32

Table 4.8: Summary of results for the smaller size of HPC

Specimen Name	S2	S3	S6	Average	Standard Deviation
l_1 (mm)	129.94	91.69	168.65	130.09	38.48
W_1 (μm)	27.24	22.68	36.77	28.89	7.19

4.1.5 Fracture Energy, G_F

For each specimen, the curve of corrected load, P_1 versus load-point displacement, δ was plotted. Then the value for δ $_A$, the intersection of the rising part of the curve with the δ axis is determined (Figure 4.7).

For each specimen, the load-point displacement $δ_R$ of the last point of the test record was determined.

Then, for each specimen, the measured work of fracture W_{Fm} as the area enclosed between the positive part of the P_1 vs. δ curve and the δ axis is calculated (Figure 4.7).

$$W_F = W_{Fm} + \frac{2A}{\delta_R - \delta_A}$$

4.11
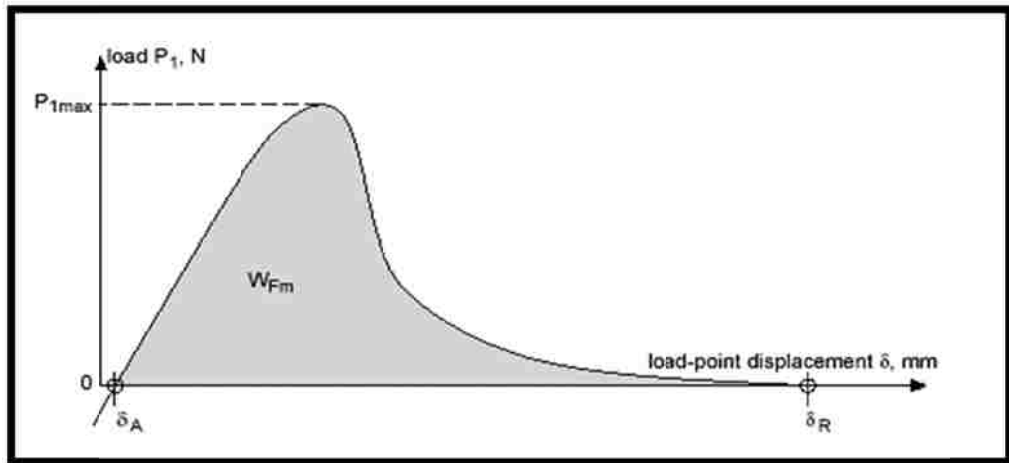
Figure 4.7: Plot of corrected load P$_1$ versus load-point displacement δ [37]

The plots for the corrected peak load versus load point displacement for all the specimens for two sizes for both UHPC and HPC are shown below:
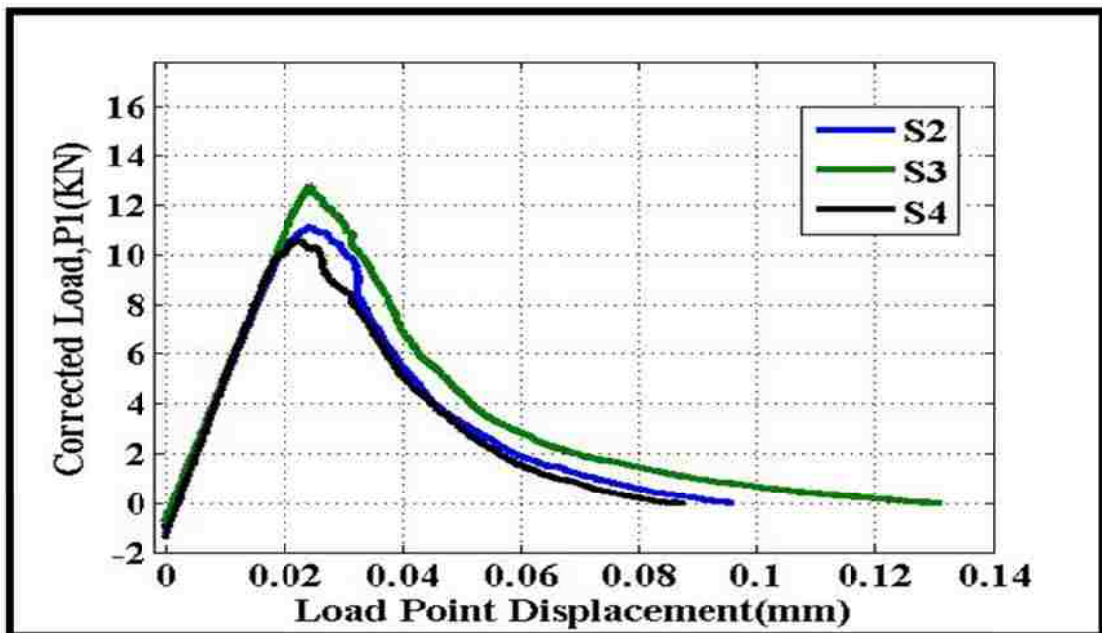
Figure 4.8: Corrected load P$_1$ versus load-point displacement for the smaller size of UHPC
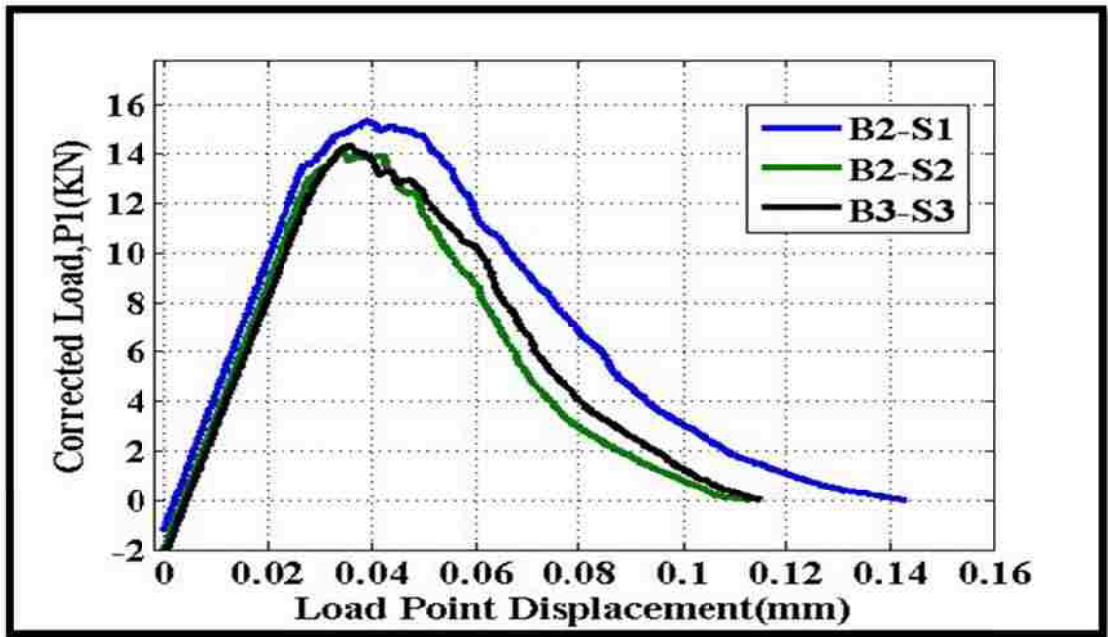
Figure 4.9: Corrected load P$_1$ versus load-point displacement for the larger size of UHPC
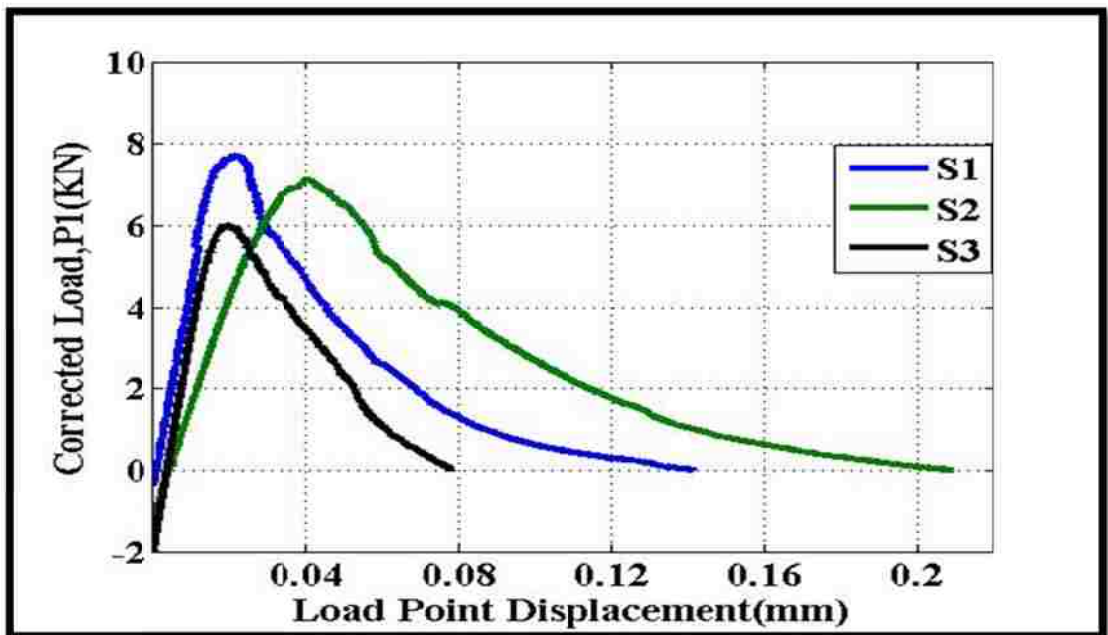
Figure 4.10: Corrected load P$_1$ versus load-point displacement for the smaller size of HPC

93
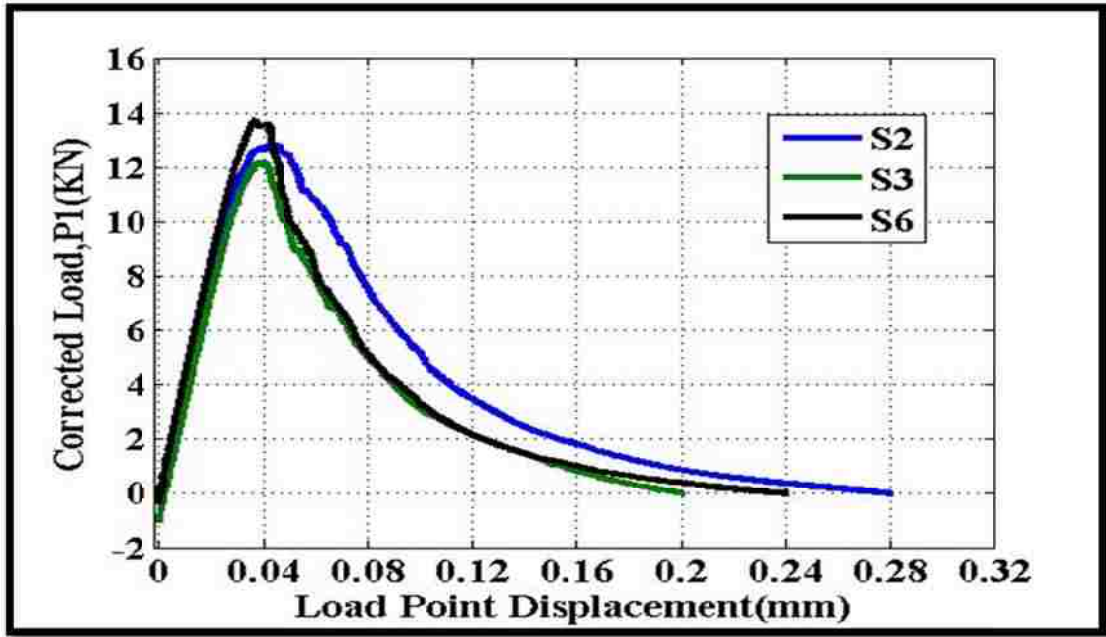
Figure 4.11: Corrected load P_1 versus load-point displacement for the larger size of HPC

Finally, the fracture energy for each specimen is calculated as follows:

$$G_F = 1000 \frac{W_F}{Bb}$$

4.12

G_F = fracture energy, N/m (J/m^2).

W_F = total work of fracture, N mm (mJ).

B = beam thickness, mm.

b = D - a_0 = ligament length, mm.

Consequently, the critical stress intensity factor, K_{IC} can also be calculated as below:

$$\mathbf{K_{IC}} = \sqrt{\mathbf{G_F E}}$$

4.13

Table 4.9: Fracture energy and stress intensity factor for the smaller size of UHPC

Specimen Name	B1-S2	B1-S3	B1-S4	Average	Standard Deviation
G_F(N/m)	92.57	94.81	65.17	84.19	16.51
K_{IC}(MPa m$^{0.5}$)	2.33	2.16	1.93	2.14	0.20

Table 4.10: Fracture energy and stress intensity factor for the larger size of UHPC

Specimen Name	B2-S1	B2-S2	B3-S3	Average	Standard Deviation
G_F(N/m)	97.12	60.72	85.00	80.95	18.53
K_{IC}(MPa m$^{0.5}$)	2.25	1.74	1.97	1.99	0.26

Table 4.11: Fracture energy and stress intensity factor for the smaller size of HPC

Specimen Name	S1	S2	S3	Average	Standard Deviation
G_F(N/m)	91.18	97.63	81.38	90.06	8.18
K_{IC}(MPa m$^{0.5}$)	1.97	2.07	1.82	1.96	0.12

Table 4.12: Fracture energy and stress intensity factor for the larger size of HPC

Specimen Name	S2	S3	S6	Average	Standard Deviation
G_F(N/m)	111.65	84.69	90.22	95.52	14.24
K_{IC}(MPa m$^{0.5}$)	2.21	1.77	1.95	1.98	0.22

4.1.6 Center of Gravity of the Softening Curve, w_G

For each specimen, the abscissa of the center of gravity of the area under the softening curve is calculated as below:

$$w_G = \frac{4A}{BSG_F} \times 10^6$$

4.14

w_G = center of gravity of the area under the softening curve, µm (microns).

A = far tail constant in N mm^2.

B = beam thickness, mm.

S = loading span, mm.

G_F = fracture energy of the specimen, N/m.

Table 4.13: w_G for the smaller size of UHPC

Specimen Name	B1-S2	B1-S3	B1-S4	Average	Standard Deviation
W_{G}(µm)	18.68	22.08	11.96	17.57	5.15

Table 4.14: w_G for the larger size of UHPC

Specimen Name	B2-S1	B2-S2	B3-S3	Average	Standard Deviation
W_G(µm)	24.02	13.94	22.84	20.27	5.51

Table 4.15: w_G for the smaller size of HPC

Specimen Name	S1	S2	S3	Average	Standard Deviation
W_G(µm)	33.48	36.49	23.52	31.16	6.79

Table 4.16: w_G for the larger size of HPC

Specimen Name	S2	S3	S6	Average	Standard Deviation
W_G(µm)	43.76	36.78	36.49	39.01	4.12

4.1.7 Bilinear Approximation of the Softening Curve

The mean values for l_1, w_1, G_F, and w_G are determined for three specimens for two different sizes. Then w_{ch} can be calculated as below:

$$w_{ch} = \frac{G_{Fm}}{f_t}$$

4.15

w_{ch} = characteristic crack opening, µm (microns).

G_{Fm} = mean fracture energy, N/m.

f_t= tensile strength, MPa.

Eventually, the critical crack opening of the bilinear approximation is evaluated as below:

$$w_c = w_{ch} \frac{3w_{Gm} - w_{1m}}{2w_{ch} - w_{1m}} \left[1 + \sqrt{1 - \frac{2w_{1m}(3w_{Gm} - 2w_{ch})(2w_{ch} - w_{1m})}{w_{ch}(3w_{Gm} - w_{1m})^2}} \right]$$

4.16

Where

w_c = critical crack opening, μm (microns).

w_{ch} = characteristic crack opening, μm (microns).

w_{Gm} = mean center of gravity of the area under the stress versus crack opening curve, μm (microns).

w_{1m} = mean horizontal intercept, μm (microns).

Also, the stress, and crack opening at the kink point can be calculated, so:

$$\sigma_k = f_t \frac{2w_{ch} - w_{1m}}{w_c - w_{1m}}$$

4.17

$$w_k = w_{1m} \frac{w_c - 2w_{ch}}{w_c - w_{1m}}$$

4.18

Where,

σ_k = stress at the kink point, MPa.

f_t = tensile strength, MPa.

w_{ch} = characteristic crack opening, μm (microns).

w_{1m} = mean horizontal intercept, μm (microns).

w_c = critical crack opening, μm (microns).

w_k = crack opening at the kink point, μm (microns).

w_c = critical crack opening, μm (microns).

The results for parameters needed to plot bilinear softening curve are shown below:

Table 4.17: Bilinear softening curve parameters for HPC

	Smaller Size	Larger Size
$w_{ch}(\mu m)$	19.58	20.77
$w_c(\mu m)$	122.59	262.26
$\sigma_k(MPa)$	0.96	0.25
$w_k(\mu m)$	13.66	27.33

Table 4.18: Bilinear softening curve parameters for UHPC

	Smaller Size	Larger Size
$w_{ch}(\mu m)$	11.53	10.49
$w_c(\mu m)$	172.75	105.27
$\sigma_k(MPa)$	0.19	0.73
$w_k(\mu m)$	18.50	11.06

Now, the bilinear softening curve can be plotted for each size of HPC and UHPC as below:
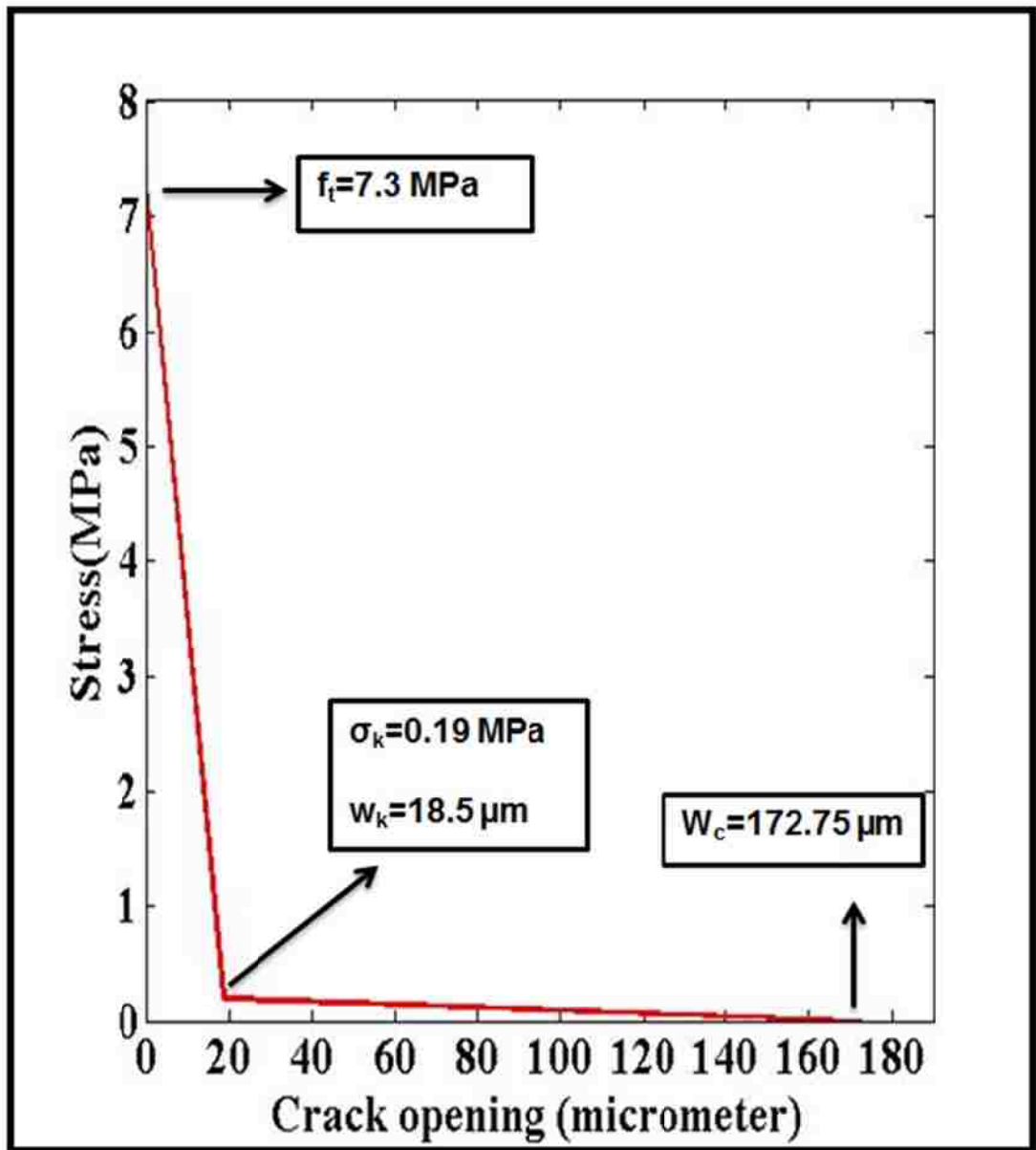
Figure 4.12: Bilinear softening curve for the smaller size of UHPC
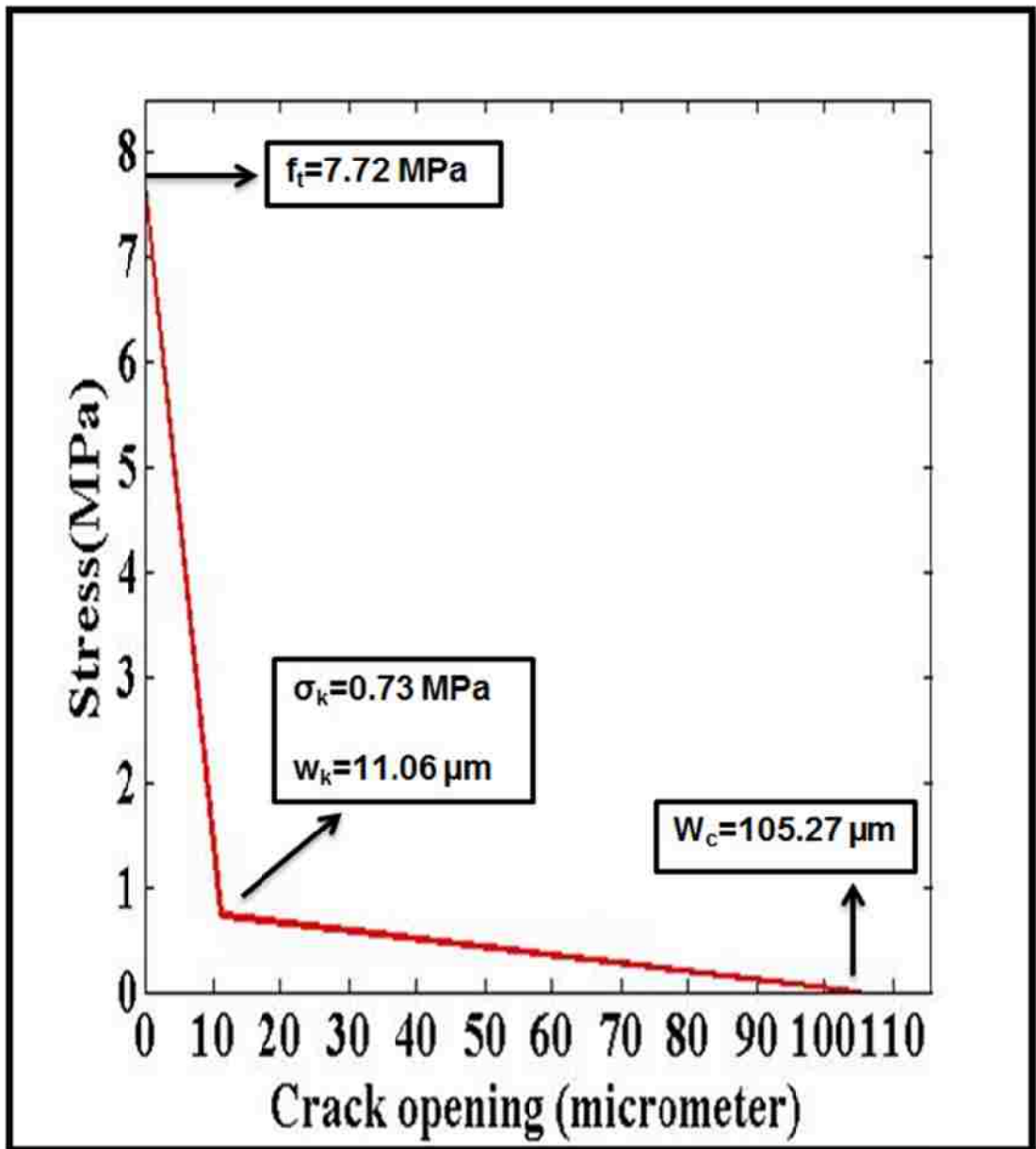
Figure 4.13: Bilinear softening curve for the larger size of UHPC
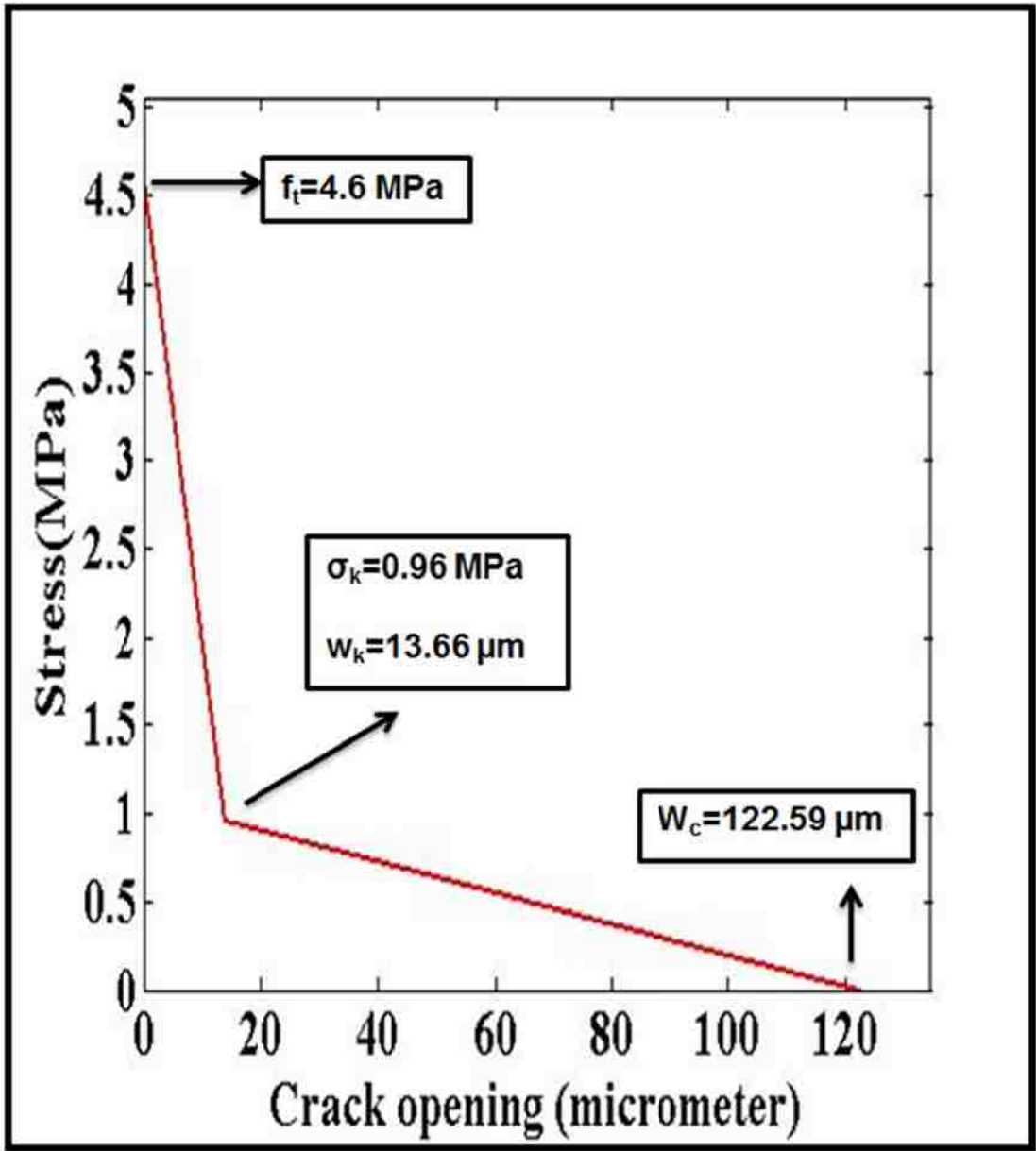
Figure 4.14: Bilinear softening curve for the smaller size of HPC
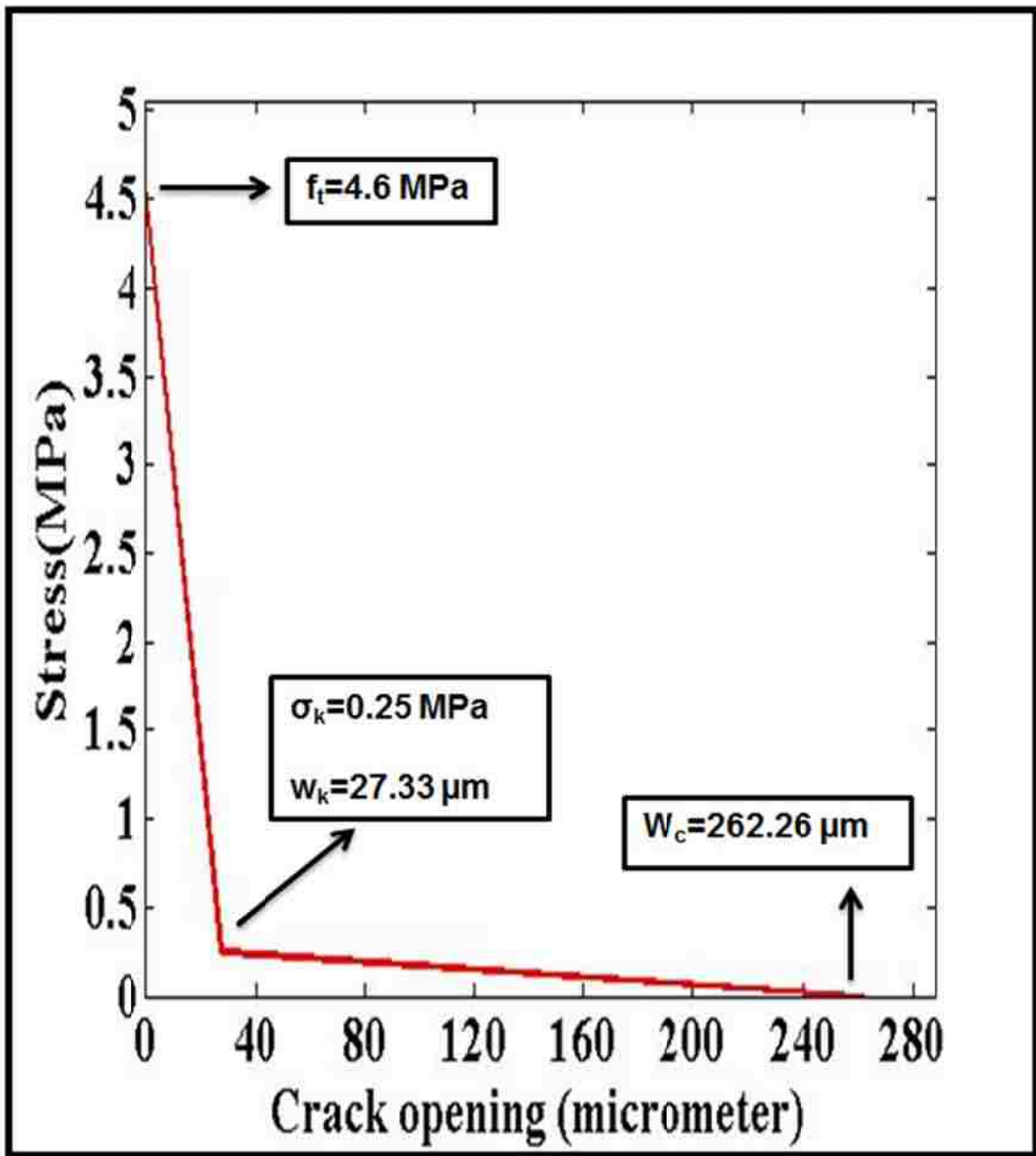
Figure 4.15: Bilinear softening curve for the larger size of HPC

The original graphs for load versus CMOD, and versus LVDT are shown below:
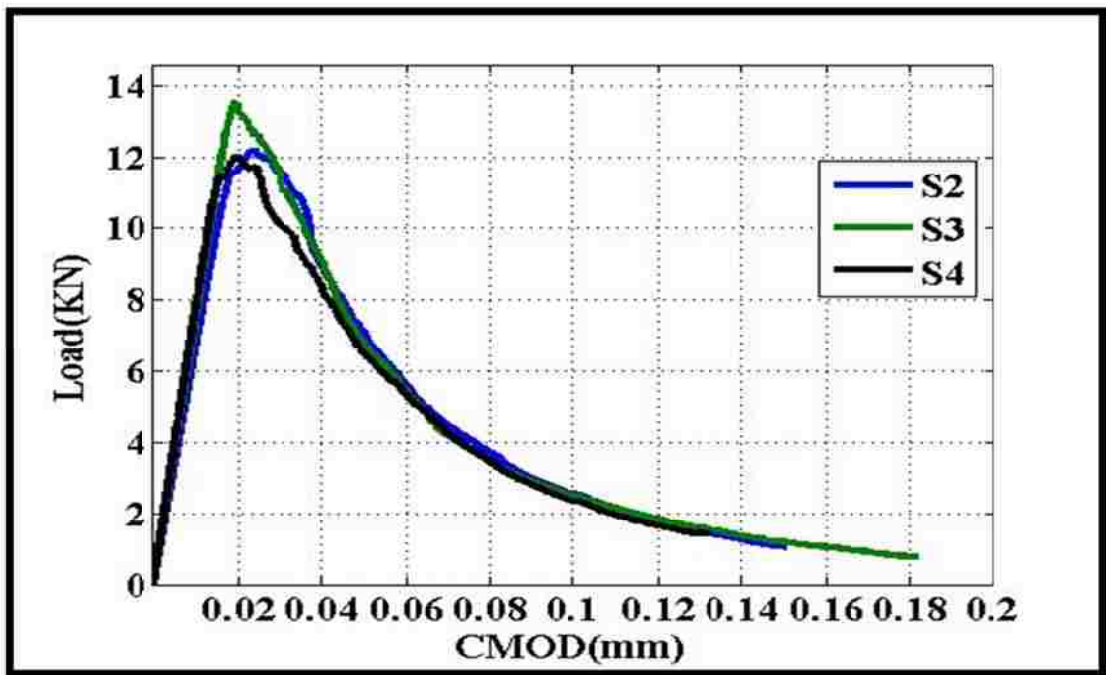
Figure 4.16: Load versus CMOD for the smaller size of UHPC specimens
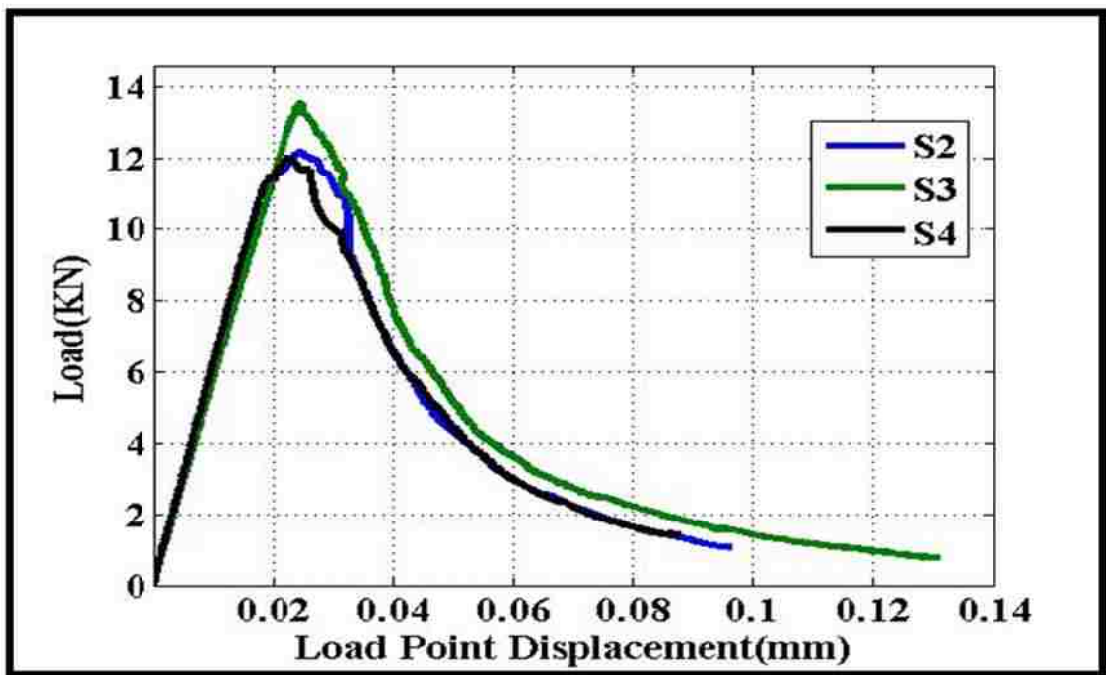
Figure 4.17: Load versus load point displacement for the smaller size of UHPC specimens
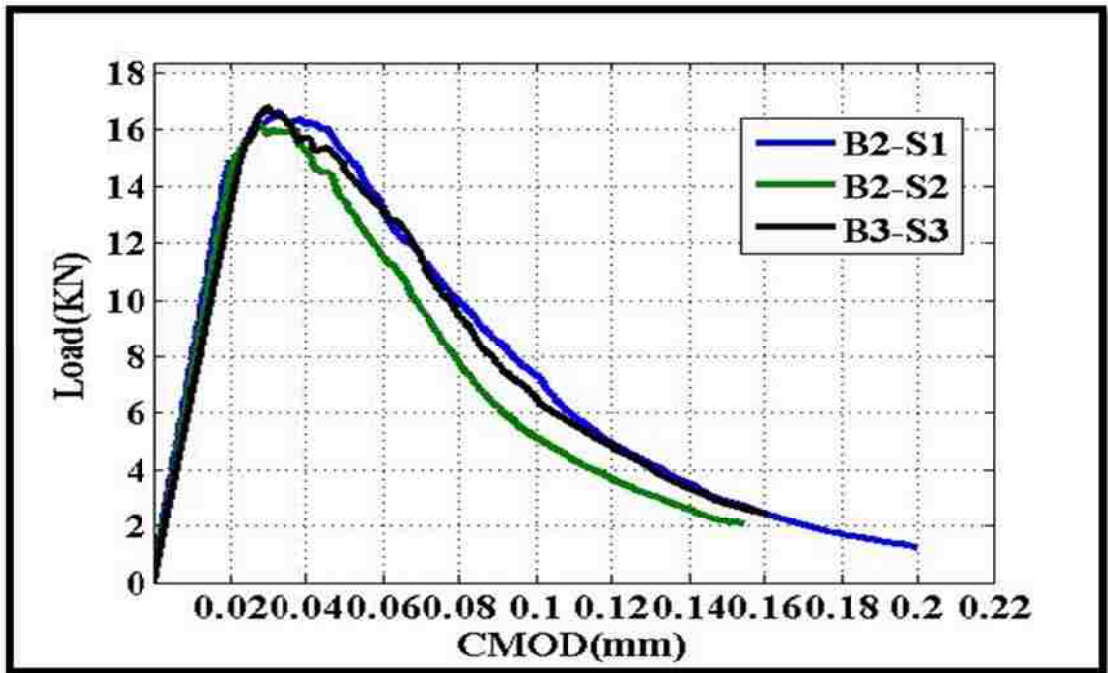
Figure 4.18: Load versus CMOD for the larger size of UHPC specimens
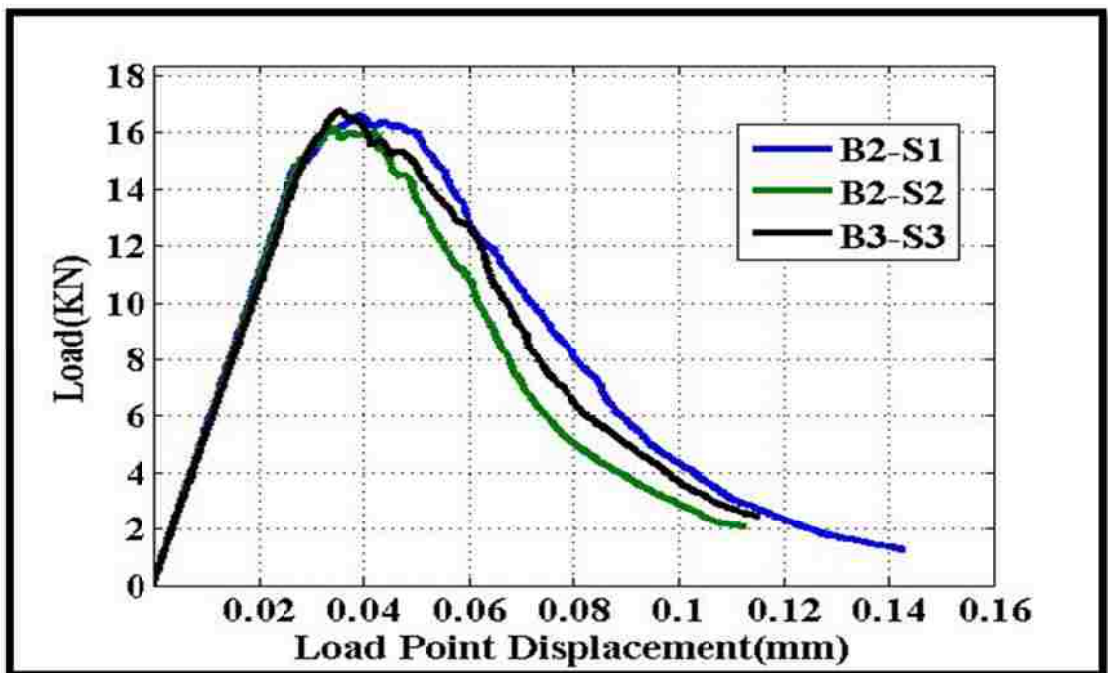
Figure 4.19: Load versus load point displacement for the larger size of UHPC specimens

105
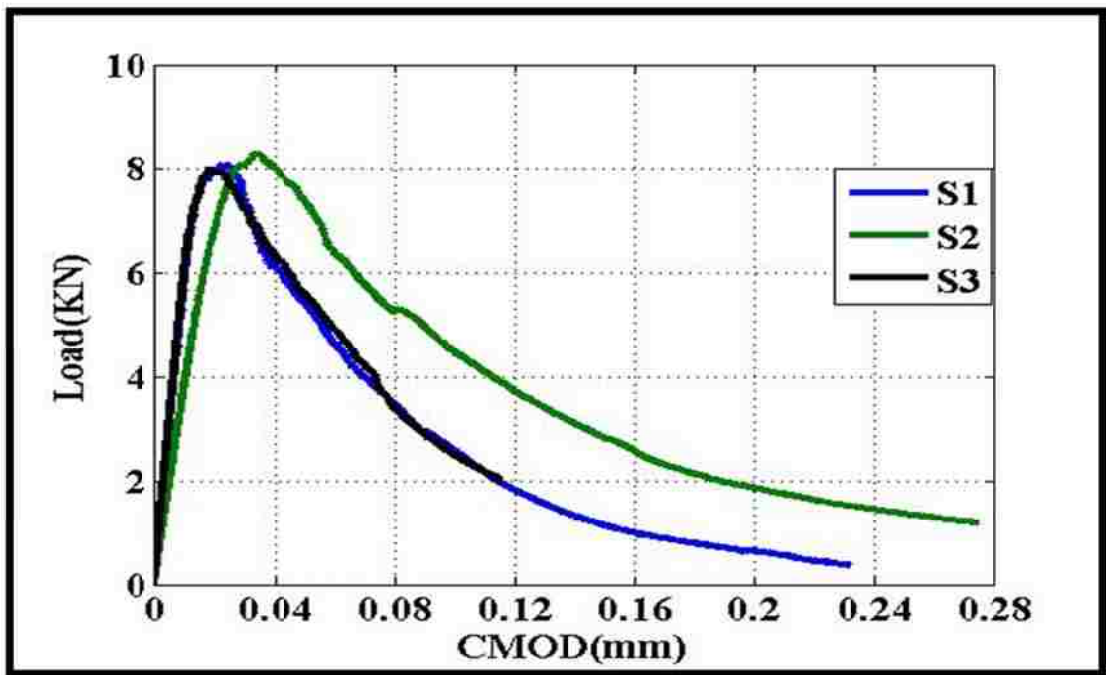
Figure 4.20: Load versus CMOD for the smaller size of HPC specimens
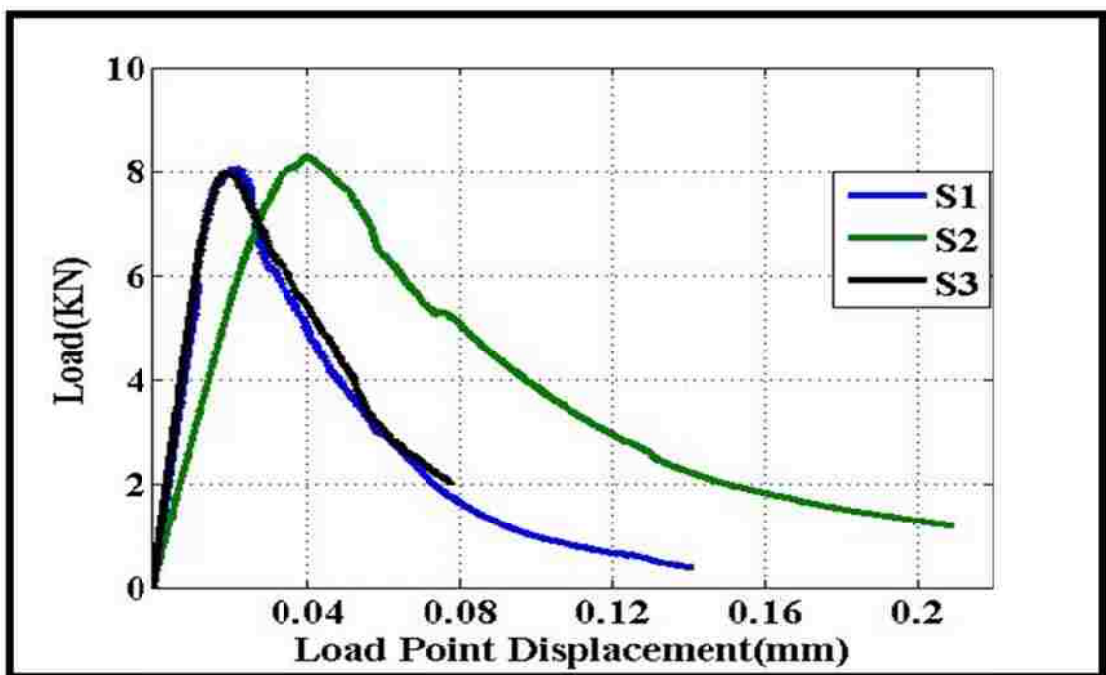
Figure 4.21: Load versus load point displacement for the smaller size of HPC specimens
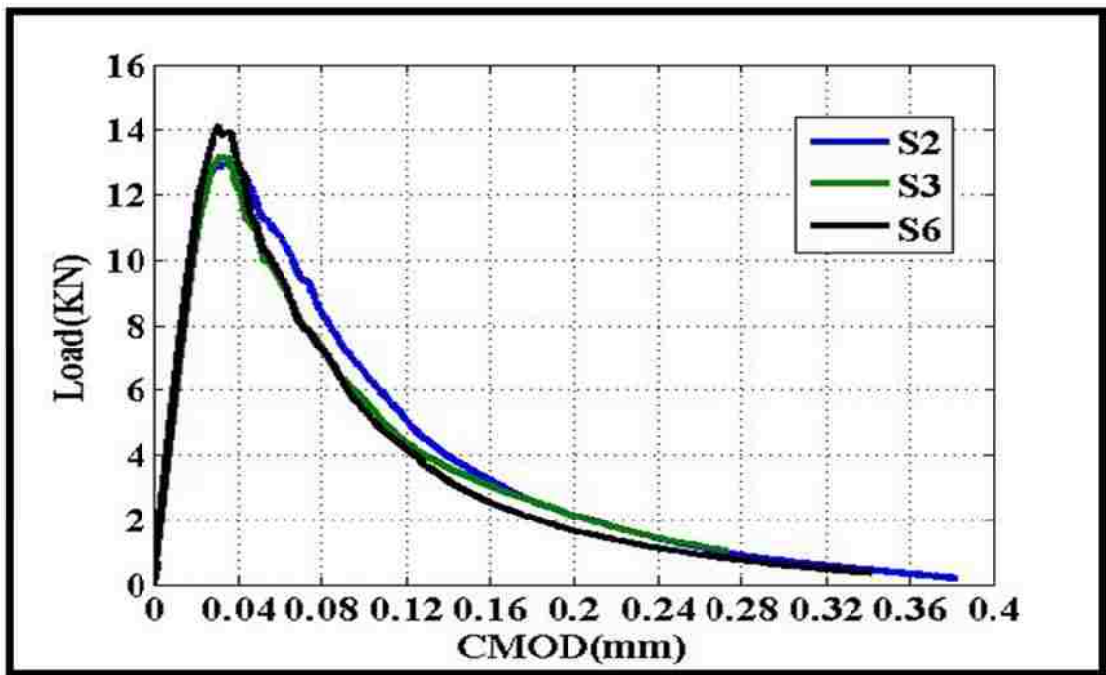
Figure 4.22: Load versus CMOD for the larger size of HPC specimens
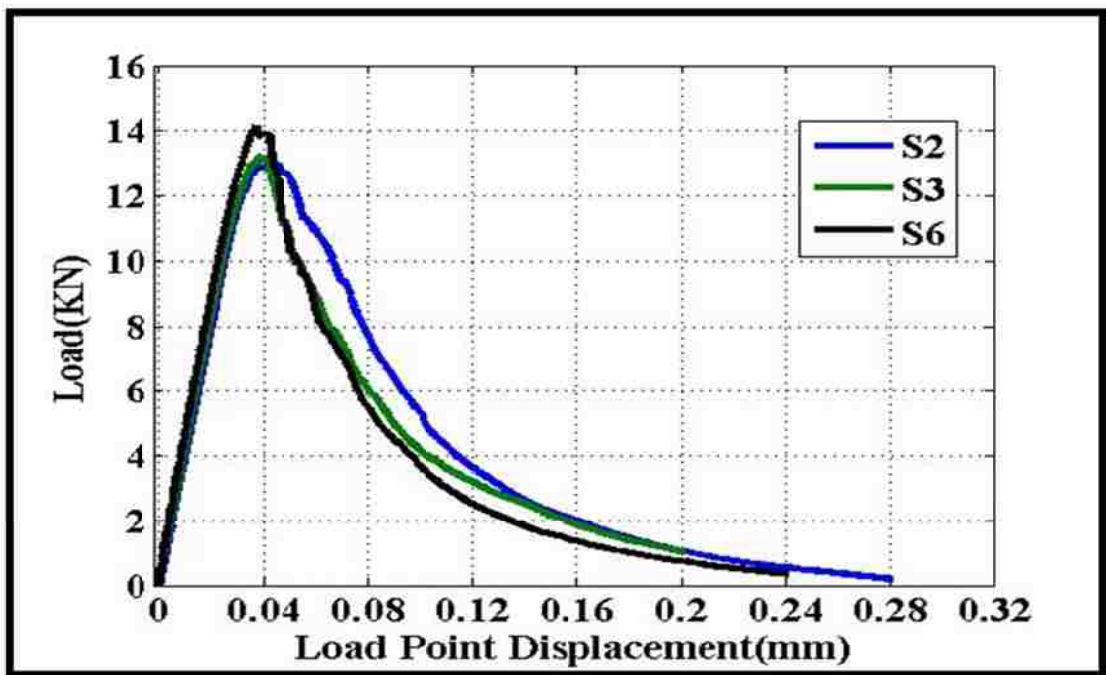
Figure 4.23: Load versus load point displacement for the larger size of HPC specimens

107

4.2 Summary of Results

The summary of all the parameters calculated earlier is tabulated below:

Table 4.19: Summary of results for the smaller size of UHPC

| Specimen name	B1-S2	B1-S3	B1-S4	Average	Standard Deviation
Peak Load (N)	12180.8	13543.3	12006.2	12576.8	841.63
W_o-CMOD at peak load (mm)	0.02376	0.01905	0.01981	0.02087	0.00253
Time for peak load (min)	4.85	4.00	4.28	4.38	0.43
P_r- Residual load(N)	1056.54	769.22	1427.29	1084.35	329.92
Time at end of test (min)	29.08	29.08	28.11	28.76	0.56
W_{MR}-CMOD at end of test(mm)	0.15029	0.18187	0.13259	0.15492	0.02497
E (MPa)	58574.4	49367.2	57021.1	54987.64	4928.94
F_p (MPa)	3.66	3.69	3.26	3.54	0.24
A (N-mm^2)	15.219	18.393	6.870	13.494	5.952
G_F (N/m)	92.57	94.81	65.17	84.19	16.51
K_{IC}(MPa m$^{0.5}$)	2.33	2.16	1.93	2.14	0.20
l_1 (mm)	118.59	125.18	73.71	105.83	28.01
W_1 (µm)	29.56	37.02	18.87	28.48	9.12
W_G(µm)	18.68	22.08	11.96	17.57	5.15

Table 4.20: Summary of results for the larger size of UHPC

Specimen name	B2-S1	B2-S2	B3-S3	Average	Standard Deviation
Peak Load (N)	16620.30	16155.61	16768.77	16514.89	319.89
W_o-CMOD at peak load (mm)	0.03242	0.02725	0.02950	0.02972	0.00259
Time for peak load (min)	4.02	3.33	3.49	3.61	0.36
P_r- Residual load(N)	1259.13	2070.60	2415.68	1915.14	593.74
Time at end of test (min)	27.02	20.16	21.73	22.97	3.59
W_{MR}-CMOD at end of test(mm)	0.19969	0.15448	0.16048	0.17155	0.02456
E (MPa)	52175.17	49777.51	45610.52	49187.74	3321.83
F_p (MPa)	2.27	2.04	2.18	2.16	0.12
A (N-mm^2)	40.816	14.810	33.979	29.868	13.481
G_F (N/m)	97.12	60.72	85.00	80.95	18.53
K_{IC}(MPa m$^{0.5}$)	2.25	1.74	1.97	1.99	0.26
l_1 (mm)	46.88	34.73	41.66	41.09	6.09
W_1 (µm)	13.12	10.19	13.33	12.21	1.76
W_G(µm)	24.02	13.94	22.84	20.27	5.51

Table 4.21: Summary of results for the smaller size of HPC

Specimen name	S1	S2	S3	Average	Standard Deviation
Peak Load (N)	8102.34	8321.47	8020.01	8174.27	200.17
W_o-CMOD at peak load (mm)	0.0234	0.033838	0.01842	0.02122	0.00255
Time for peak load (min)	4.88	3.24	3.81	4.44	0.56
P_r- Residual load(N)	362.55	1190.75	1984.91	962.07	890.17
Time at end of test (min)	22.67	20.53	17.21	21.47	3.81
W_{MR}-CMOD at end of test(mm)	0.2319086	0.2746	0.11526	0.19698	0.07103
E (MPa)	42734.88	43893.64	40802.32	42476.95	1561.72
F_p (MPa)	2.24	2.20	1.97	2.14	0.15
A (N-mm^2)	26.990	28.440	16.968	24.133	6.247
G_F (N/m)	91.18	97.63	81.38	90.06	8.18
K_{IC}(MPa m$^{0.5}$)	1.97	2.07	1.82	1.96	0.12
l_1 (mm)	72.39	101.43	65.93	79.92	18.91
W_1 (µm)	18.04	19.50	14.87	17.47	2.37
W_G(µm)	34.53	36.49	23.52	31.51	6.99

Table 4.22: Summary of results for the larger size of HPC

Specimen name	S2	S3	S6	Average	Standard Deviation
Peak Load (N)	13002.58	13197.85	14141.6	13447.3	609.12
W_o-CMOD at peak load (mm)	0.03458	0.03150	0.03058	0.03222	0.00209
Time for peak load (min)	4.86	3.75	3.58	4.06	0.70
P_r- Residual load(N)	184.14	1036.50	355.85	525.50	450.79
Time at end of test (min)	23.58	21.20	22.77	22.52	1.21
W_{MR}-CMOD at end of test(mm)	0.38239	0.27284	0.34105	0.33210	0.0553
E (MPa)	43894.3	37199.4	42199.9	41097.9	3480.8
F_p (MPa)	1.97	1.78	2.12	1.96	0.17
A (N-mm^2)	86.213	55.331	56.630	66.058	17.467
G_F (N/m)	111.65	84.69	90.22	95.52	14.24
K_{IC}(MPa m$^{0.5}$)	2.21	1.77	1.95	1.98	0.22
l_1 (mm)	129.94	91.69	168.65	130.09	38.48
W_1 (µm)	27.24	22.68	36.77	28.89	7.19
W_G(µm)	43.76	36.78	36.49	39.01	4.12

4.3 Discussion

4.3.1 Bilinear Softening Curve

The bilinear softening curves for two different sizes for UHPC are sketched in Figure 4.24. It is observed that the critical crack opening displacement for size1, which is the smaller size of beam, is more than that for the larger size of beams. This can be justified by the fact that, as the specimen increases in size, it becomes more brittle, a phenomenon which is even more pronounced in UHPC. Although the stress at the kink point is much higher for the larger size than the smaller size, overall, both sizes exhibits the same trend of softening, since their slopes of the first segment of the bilinear curve are very close.
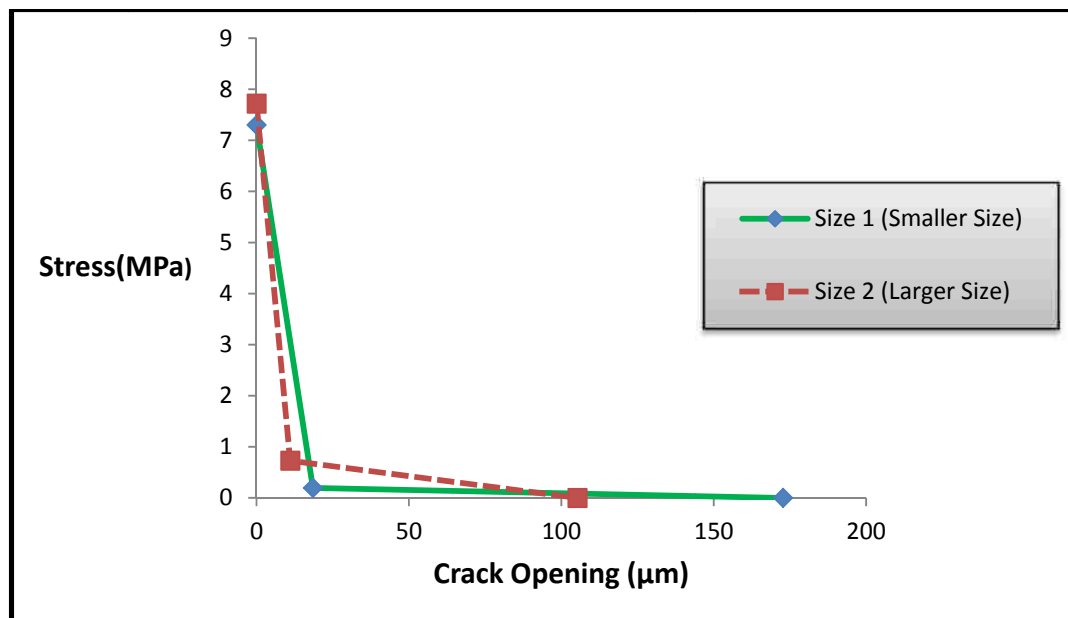
Figure 4.24: Bilinear softening curves for two different sizes of UHPC

The bilinear softening curves for two different sizes for HPC are sketched in Figure 4.25. Unlike UHPC, it is observed that, the critical crack opening displacement for the larger size is almost twice the smaller size. Yet, the stress at the kink point for smaller size is higher than that of the larger size. HPC is not as brittle as UHPC, so the bigger size of beam contributes to more opening of the crack.
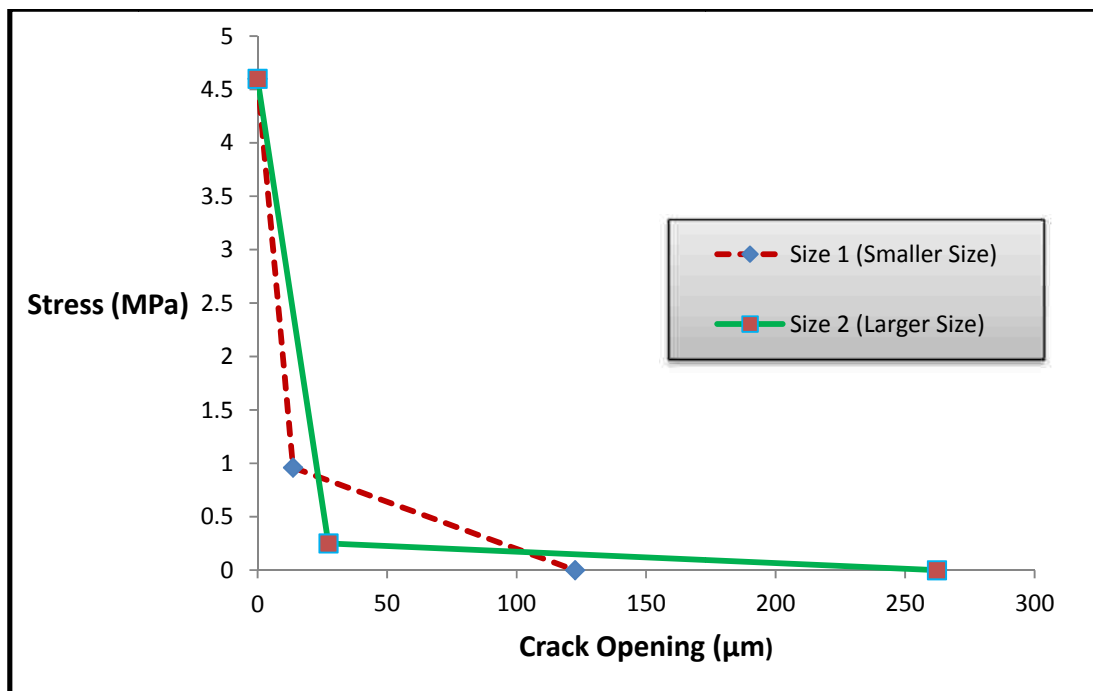
**Figure 4.25: Bilinear softening curves for two different sizes of HPC**

Finally, Figure 4.26 helps realize how the softening curve of concrete behaves with changes in size and compressive strength of concrete. It is observed that the larger size of HPC, which is a bigger beam, with lower compressive strength has the largest value for critical crack opening displacement, while the larger size

of UHPC, which is the bigger beam, with higher compressive strength has the lowest value for critical crack opening displacement. It is also interesting to see that, smaller size of UHPC has a bigger value of critical crack opening displacement than smaller size of HPC. In other words, higher strength of concrete contributes to better softening curve for concrete for smaller size of the beam, whereas this is not the case for larger beams; concrete with lower strength behaves more properly in terms of softening by indicating larger critical crack opening displacement. Comparison of softening also reveals that, the change trend in stress at kink point is different for HPC and UHPC for the two sizes. The larger size of HPC has lower stress than smaller size at kink point, while, the larger size of UHPC has higher stress than the smaller size. Besides, the highest value for stress at kink point is observed for the smaller size of HPC.
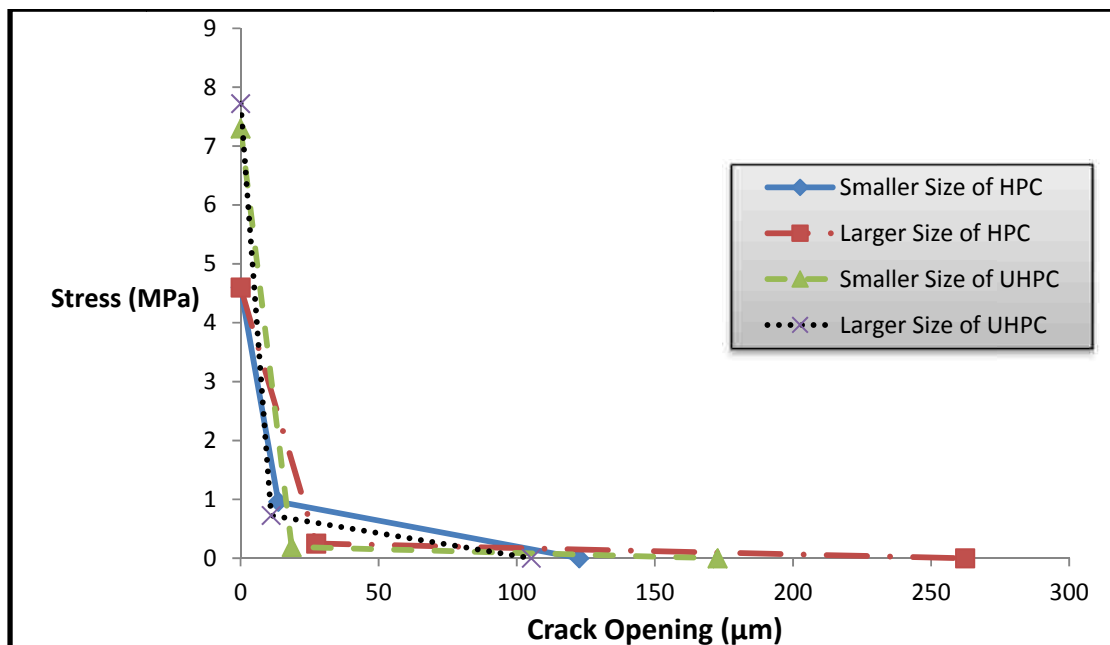

Figure 4.26: Bilinear softening curves for two different sizes of UHPC, and HPC

4.3.2 Critical Crack Opening Displacement

The table below summarizes the values of the critical crack opening displacement for two different sizes of UHPC, and HPC. It also demonstrates how much these values differ from each other. It is observed that the values of the critical crack opening displacement were different for the two different sizes of beams.

Table 4.23: Comparison of critical crack opening displacement of two different sizes for HPC, and UHPC

	HPC			UHPC		
	Smaller Size	Larger Size	Difference (%)	Smaller Size	Larger Size	Difference (%)
$COD_c(\mu m)$	122.59	262.26	-113.9	172.75	105.27	39.1

4.3.3 Fracture Energy and Critical Stress Intensity Factor

The scatter in the data for fracture energy, G_F and critical stress intensity factor, K_{IC} versus compressive strength of concrete for two sizes for both UHPC, and HPC is sketched in Figure 4.27. It is observed that the fracture energy decreases significantly as the compressive strength increases for the larger size, while the loss in the fracture energy due to increase in compressive strength is insignificant and negligible for the smaller size. CEB –FIP 90 has predicted a different trend in fracture energy for concrete with the compressive strength ranging from 12 to 80

MPa; it was shown that for different maximum size of aggregates, the fracture energy increases as the compressive strength increases [**30**].

Furthermore, for a specific strength of concrete, the two sizes demonstrate almost the same value for fracture energy, demonstrating size independency, which was expected according to the test method proposed by ACI Committee 446.

Table 4.24: Comparison of fracture energy of two different sizes for HPC, and UHPC

	HPC			UHPC		
	Smaller Size	Larger Size	Difference (%)	Smaller Size	Larger Size	Difference (%)
G_F (N/m)	90.06	95.52	-6	84.19	80.95	4

Table 4.25: Comparison of fracture energy for UHPC and HPC for two different sizes

	Smaller Size			Larger Size		
	HPC	UHPC	Difference (%)	HPC	UHPC	Difference (%)
G_F (N/m)	90.06	84.19	6.5	95.52	80.95	15.3

However, for critical stress intensity factor, a different trend is observed. The increase in values for K_{IC} is not significant as the compressive strength increases for two different sizes. Hence, the changes in fracture toughness for two different strengths are negligible.

Moreover, if the strength of concrete is held constant, the increase in size of the beam does not vary the values of fracture toughness either HPC or UHPC. Thus, no size effect exists in determining the value of fracture toughness.

Table 4.26: Comparison of critical stress intensity factor of two different sizes for HPC, and UHPC

	HPC			UHPC		
	Smaller Size	Larger Size	Difference (%)	Smaller Size	Larger Size	Difference (%)
K_{IC}(MPa m$^{0.5}$)	1.96	1.98	-1.26	2.14	1.99	7.18

Table 4.27: Comparison of critical stress intensity factor for UHPC and HPC for two different sizes

|	Smaller Size			Larger Size		
	HPC	UHPC	Difference (%)	HPC	UHPC	Difference (%)
K_{IC}(MPa m$^{0.5}$)	1.96	2.14	-9.1	1.98	1.99	-0.5
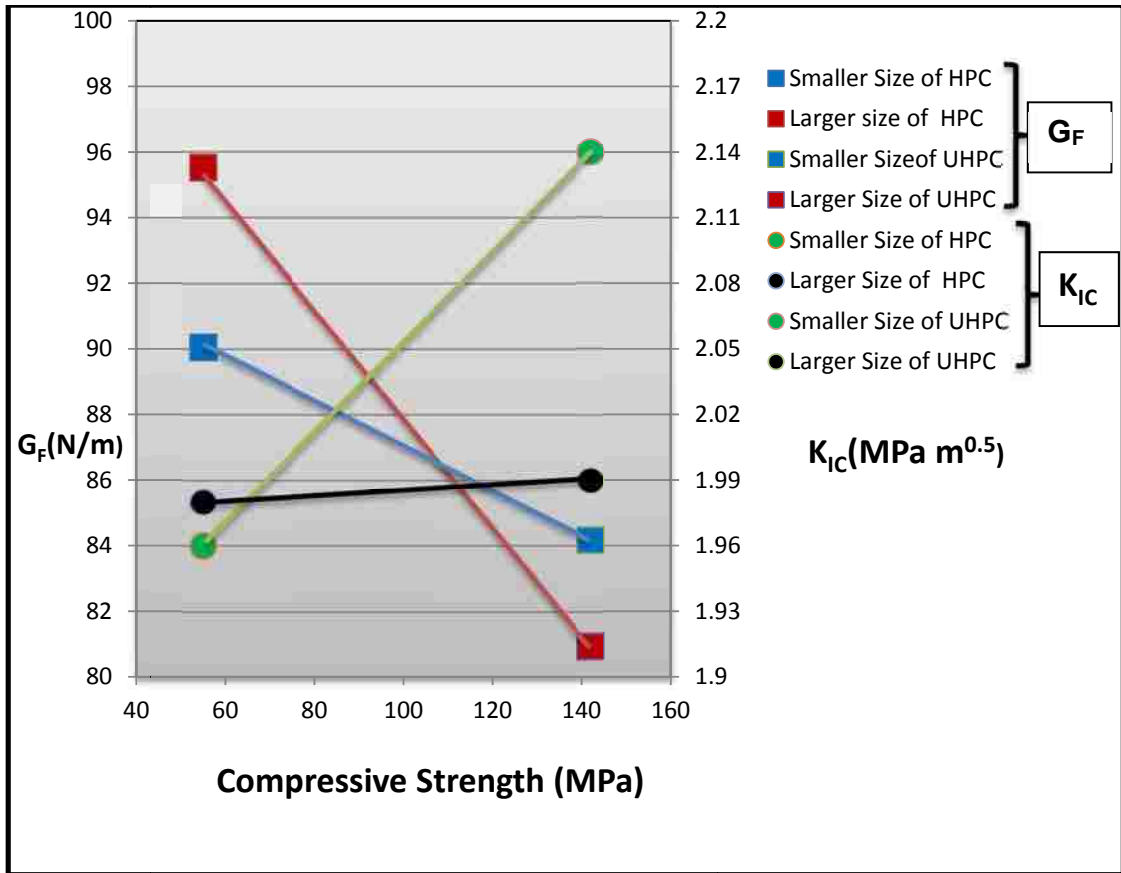
Figure 4.27: Variation of fracture enregy and critical stress intensity factor versus compressive strength for UHPC and HPC for two different sizes.

CHAPTER 5

5 CONCLUSIONS

5.1 Conclusions

Study of the fracture parameters of ultra-high performance concrete (UHPC), and high performance concrete (HPC) based on the test method proposed by ACI Committee 446, has led to several conclusions:

- UHPC with no fibers and HPC don't generally exhibit high fracture toughness compared to normal strength concrete due to their intrinsic brittleness, in spite of high compressive strength.

- Values of fracture energy G_F, and fracture toughness K_{IC} for two different sizes are very close, which indicate that the property was size independent for two different sizes, as per the method proposed by ACI committee 446.

- For the smaller size of beams (size1), increase in compressive strength led to a negligible decrease in fracture energy. However, the fracture energy decreased significantly for the larger beams.

- HPC exhibits more ductile behavior than UHPC for the bigger size, whereas UHPC indicates more ductile behavior than HPC for the smaller

119

size. The extension of the tail end of the softening curve is an indication of ductile fracture behavior.

- ACI Committee 446 test method was successfully applied to determine the fracture parameters of two types of high and ultra-high strength concrete. However, some difficulties still exist in determining a proper loading pattern for CMOD increase rate to get a good softening curve for highly brittle materials such as UHPC, which warrants a thorough revision of ACI Committee 446 loading pattern.

REFERENCES

[1] A. Hillerborg, M. Modee, and P. E. Petersson, "Analysis of crack formationand crack growth in concrete by means of fracture mechanics and finite elements," *Cement and concrete research*, vol. 6, no. 6, pp. 773-782, 1976.

[2] J. Xiao, H. Schnieder, and C. Donnecke, "Wedge spliting test on fracture behavior of ultra high strength concrete," *Construction and building materials*, vol. 18, no. 359-365, 2004.

[3] J. C. Walraven, "Ultra-hogesterktebeton," *een material in ontwikkeling. In: Cement (Dutch)*, vol. 5, pp. 57-61, 2006.

[4] Bache, "Densified cement/ultra fine particle based materials," in *Second International Conference on Superplasticizers in Concrete*, Ottawa, Ontario, Canada, 1981.

[5] Buitelaar, "Heavy Reinforced Ultra High Performance Concrete," in *Proceedings of the International Symposium on Ultra High Performance Concrete*, Kassel University Press, Kassel, Germany. , 2004.

[6] P. Acker and Behloul, "Ductal Technology: a Large Spectrum of Properties, a Wide Range of Applications," in *International Symposium on Ultra High Performance Concrete*, Kassel University Press, Kassel, Germany, 2004, pp. 11-24.

[7] M. Schmidt, E. Fehling, T. Teichmann, K. Bunje, and R. Bornemann, "Ultra high performance concrete: Perspective for the precast concrete industry," *Beton und Fertigteil-Technik*, vol. 3, pp. 16-29, 2003.

[8] Z. Hajar, A. Simon, D. Lecointre, and J. Petitjean, "Design and Construction of the world first Ultra-High Performance road bridges," in *International*

Symposium on Ultra High Performance Concrete, Kassel University Press, Kassel, Germany, 2004, pp. 39-48.

[9] J. Resplendino, "First Recommendations for Ultra-High-Performance Concretes and examples of Application," in *International Symposium on Ultra High Performance Concrete*, Kassel University Press, Kassel, Germany, 2004, pp. 79-90.

[10] ACI Committee 363, "State-of-the-Art Report on High-Strength concrete," American Concrete institute 363R-92, 1997.

[11] T. L. Anderson, *Fracture Mechanics*, 3rd ed. CRC press, 2005.

[12] Griffith, "The phenomena of rupture and flow in solids," *Philosophical transaction, royal society of London*, vol. 221, pp. 163-197, 1920.

[13] Orowan, "Energy criteria for fracure," *Welding journal*, vol. 34, pp. 1575-1605, 1955.

[14] G. R. Irwin, "Plastic zone near a crack and fracture toughness," in *Sagamore research conference*, Syracuse university research institute, Syracuse NY, 1961, pp. 63-78.

[15] A. A. Wells, "Unstable crack propagation in metals: Cleavage and fast fracture," in *crack propagation symposium*, cranfield UK, 1961.

[16] J. R. Rice, "A path independent integral and the approximate analysis of stress concentration by notches and cracks," *Journal of Applied Mechanics*, vol. 35, pp. 379-386, 1968.

[17] S. P. Shah, S. E. Swartz, and C. Ouyang, *Fracture mechanics of concrete: Application of fracture mechanics to concrete, rock, and other quasi-brittle materials*. John Wiley & Sons Inc., 1995.

[18] E. Z. Wang and N. G. Shrive, "Brittle fracture in compression: mechanisms, models, and criteria," *Engineering fracture mechanics*, vol. 52, no. 6, pp. 1107-1126, 1995.

[19] A. A. Griffith, "The theory of rupture," in *International congress on applied physics*, Delft, 1924, pp. 55-63.

[20] S. Midess and S. Diamond, "The cracking and fracture of mortar," *Materiaux et constructions*, vol. 15, no. 86, pp. 107-113, 1982.

[21] B. N. Cox and D. B. Marshall, "Concepts for bridged cracks in fracture and fatigue," *Acta Metallurgy*, vol. 42, no. 2, pp. 341-363, 1994.

[22] J. Glucklich, "Fracture of plain concrete," in *American society of civil engineers*, vol. 89, 1963, pp. 127-138.

[23] F. Moavenzadeh and R. Kuguel, "Fracture of concrete," *Journal of materials*, vol. 4, pp. 497-519, 1969.

[24] S. Mindess, "The fracture of fiber reinforced and polymer impregnated concretes: A review," in *Fracture mechanics of concrete*. Amsterdam: Elsevier Science, 1983, ch. 6, pp. 481-501.

[25] A. N. Kumar, "Effect of physical crack growth on CTOD measurement," *international journal of fracture*, vol. 35, no. 5, pp. 813-826, 1987.

[26] J. R. Rice, P. C. Paris, and J. G. Merkle, "Some further results of J-integral alanysis and estimates," American Soceity of Testing and Materials ASTM STP 536, 1973.

[27] S. Mindess, F. V. Lawrence, and C. E. Kesler, "The J-integral as a fracture criterion for fiber reinforced concrete," *Cement and concrete research*, vol. 7, no. 6, pp. 731-742, 1977.

[28] D. S. Dugdale, "Yielding of steel sheets contatinig silts," *Journal of mechanics, physics, and solids*, vol. 8, pp. 100-104, 1960.

[29] G. J. Barenblatt, "The mathematical Theory of Equilibrium crack in the brittle fracture," *Advances in applied mechanics*, vol. 7, pp. 55-125, 1962.

[30] "Model code for concrete structures," Comite Euro-international du beton (CEB)- Federation internationale de la precontrainte (FIP) CEP-FIP Model code 90, 1990.

[31] Y. S. Jenq and S. P. Shah, "Two parameter fracture model for concrete," *Journal of engineering mechanics*, vol. 111, no. 4, pp. 1227-1241, 1985.

[32] K. S. Tae, Y. Lee, Y.-D. Park, and J.-K. Kim, "Tensile fracture properties of an Ultra High Performance Fiber Reinforced Concrete (UHPFRC) with steel fiber," *Composite Structures*, vol. 92, pp. 61-71, 2010.

[33] T. Stengel, "FRACTURE TOUGHNESS OF STEEL FIBRE REINFORCED ULTRA HIGH PERFORMANCE CONCRETE," in *7th EUROMECH Solid Mechanics Conference*, Lisbon, Portugal,, 2009.

[34] RILEM Committee on fracture mechanics of concrete, "Determination of the fracture energy of mortar and concrete by means of three-point bens tests on notched beams," *Material and structures*, vol. 18, no. 106, pp. 285-290, 1985.

[35] Z. P. Bazant and M. T. Kazemi, "Determination of fracture energy, process zone length and brittleness number for size effect with an application to rock and concrete," *Internatinal journal of fracture*, vol. 44, pp. 111-131, 1990.

[36] S. P. Shah, "Fracture toughness of cement based materials," *Materials and structures*, vol. 21, no. 122, pp. 145-150, 1988.

[37] "Fracture Toughness Testing of Concrete," ACI Committee 446, 2009.

[38] G. V. Guinea, J. Planas, and M. Elices, "A General Bilinear Fitting for the Softening Curve of Concrete.," *Material and Structures*, vol. 27, pp. 99-105, 1994.

[39] Bazant and J. Planas, *Fracture and size effect in concrete and other quasibrittle materials*. 1997.

[40] P. E. Petersson, "Crack growth and development of fracture zone in plain concrete and similar materials," Division of building materials, Lund institute of technology TVBM-1006, 1981.

[41] M. M. Reda, N. G. Shrive, and J. E. Gillott, "Microstructural investigation of innovative UHPC," *Cement and Concrete Research*, vol. 29, pp. 323-329, 1999.

[42] B. A. Graybeal, "Material property characterization of Ultra High Performance Concrete," Federal Highway Administration, Final Report, October 2002–December 2005 FHWA-HRT-06-103, 2006.